



Topology optimization of microvascular composites for active-cooling applications using a geometrical reduced-order model

Pejman, Reza; Sigmund, Ole; Najafi, Ahmad Raeisi

Published in:
Structural and Multidisciplinary Optimization

Link to article, DOI:
[10.1007/s00158-021-02951-x](https://doi.org/10.1007/s00158-021-02951-x)

Publication date:
2021

Document Version
Peer reviewed version

[Link back to DTU Orbit](#)

Citation (APA):
Pejman, R., Sigmund, O., & Najafi, A. R. (2021). Topology optimization of microvascular composites for active-cooling applications using a geometrical reduced-order model. *Structural and Multidisciplinary Optimization*, 64, 563–583 . <https://doi.org/10.1007/s00158-021-02951-x>

General rights

Copyright and moral rights for the publications made accessible in the public portal are retained by the authors and/or other copyright owners and it is a condition of accessing publications that users recognise and abide by the legal requirements associated with these rights.

- Users may download and print one copy of any publication from the public portal for the purpose of private study or research.
- You may not further distribute the material or use it for any profit-making activity or commercial gain
- You may freely distribute the URL identifying the publication in the public portal

If you believe that this document breaches copyright please contact us providing details, and we will remove access to the work immediately and investigate your claim.

Topology optimization of microvascular composites for active-cooling applications using a geometrical reduced-order model

Reza Pejman · Ole Sigmund · Ahmad Raeisi Najafi

Received: date / Accepted: date

Abstract In this study, we develop a design methodology with a basis in gradient-based topology optimization and a geometrical reduced-order thermal/hydraulic model for actively-cooled microvascular composite panels. The proposed method is computationally very efficient owing to the suggested simplifications while preserving the required accuracy. The analytical sensitivity for the topology optimization scheme is derived. Several numerical examples are solved to demonstrate the applicability of the proposed method for active-cooling applications. Using topology optimization, the maximum temperature of the composite panel is reduced by up to 59% compared to a benchmark design. The optimization framework is compared to hybrid topology/shape (HyTopS) and shape optimization (SO) methods based on several measures such as maximum and average temperatures, temperature uniformity, network redundancy, and manufacturability. The solution obtained from the proposed TO scheme outperforms the other approaches in terms of the aforementioned measures.

Keywords Topology optimization · Microvascular composite · Cooling · Thermal management

R. Pejman
Department of Mechanical Engineering and Mechanics, Drexel University, Philadelphia, PA 19104, USA

O. Sigmund
Section for Solid Mechanics, Department of Mechanical Engineering, Technical University of Denmark, Nils Koppels Alle, Building 404, Kongens Lyngby, Denmark

A. R. Najafi
Department of Mechanical Engineering and Mechanics, Drexel University, Philadelphia, PA 19104, USA
Corresponding author:
E-mail: arn55@drexel.com

1 Introduction

Inspired by nature, microvascular fiber-reinforced composites use microchannels (i.e. vasculature) to provide conduits for circulation of fluid [1]. This unique feature offers multifunctionality to the host material based on a choice of fluid flowing through the vasculature such as thermal, electrical, self-healing, etc. In this study, we concentrate on the thermal management capability of microvascular composites, which has a wide range of applications including aerospace vehicles, battery packaging, heat exchangers, and electronic devices [2–4]. Due to the developments in science and technology, there is an increasing demand for systems to perform in higher clock speeds and power ranges. As a result, there is a rising trend in the amount of heat generated. Thus, it is of great importance to come up with new designs to improve the efficiency and performance of thermal management systems. This study is an effort to provide a systematic approach for the design optimization of microvascular composites for thermal management purposes.

In the literature, various design optimization techniques have been used to find the optimized configuration of thermal management systems such as parametric studies, evolutionary algorithms, constructal theory, and gradient-based approaches [5–14]. The method of choice in this study is the gradient-based optimization scheme, which can be classified into two main categories: shape and topology optimization. These two gradient-based methods have been widely used for the design optimization of thermal and hydraulic systems [15–29]. For instance, Jarrett et al. used gradient-based shape optimization (SO) method to optimize the cooling plate in the batteries of an electric vehicle [30]. Gradient-based topology optimization (TO) has been used to optimize the cooling network using Stokes flow [31], Navier-stokes flow [32], Darcy flow [33], and Darcy-Stokes flow [34].

Tan et al. [3] recently proposed a gradient-based shape optimization method for actively-cooled microvascular composites, which builds upon the Eulerian-based shape optimization scheme proposed by Najafi et al. [35–37]. Their method is computationally efficient since they used a geometrical reduced-order (GRO) thermal and hydraulic model and fully analytical shape sensitivity analysis over a fixed mesh in the interface-enriched generalized finite element method (IGFEM) framework [38, 39]. In this method, they collapsed the microchannels into line source/sinks and by using IGFEM, they precisely capture the microchannel boundaries in the cooling network. While insightful, their method has two crucial limitations: (i) similar to the other shape optimization approaches, the design space is confined by the topology of the initial design, and (ii) due to imposing many manufacturing constraints on their shape optimization problem, design space gets limited. Note that if the microchannels get very close to each other, it can lead to issues such as leakage in the microchannel network. This is the reason that these constraints needed to be imposed in their optimization framework.

To address the first limitation, Pejman et al. recently proposed a Hybrid Topology/Shape (HyTopS) optimization scheme [40], which can perform the topological change of the vascular network during the shape optimization process. The method was also applied to solve the HyTopS optimization of actively-cooled microvascular composites under any source of uncertainty [41]. This task is accomplished by combining the HyTopS optimization scheme with the non-intrusive polynomial chaos expansion method to create a reliable/robust microchannel network design in a microvascular composite. The HyTopS method has also been extended to design a blockage-tolerant cooling network [42]. Even though the design space is expanded in the HyTopS scheme in comparison with the SO method, it still suffers from many limitations in the design space due to imposing many manufacturing constraints on the optimization problem. We will discuss this issue further in Section 4.2.

In this study, we aim to address the issue associated with the limitation of the design space due to the manufacturing constraints imposed in our HyTopS optimization method [40] and SO method proposed in [3]. To do so, we present a topology optimization scheme for actively-cooled microvascular composites. In this method, we use the same idea as the truss topology optimization and define our lumped microchannels on the boundaries of the elements as it will be discussed in detail in Section 3. It is worth noting that this study is different from the previous work where we introduced the HyTopS optimization method [40]. First and foremost, the derivation and implementation of the sensitivity analysis in our suggested TO scheme are much simpler than in the HyTopS method. Indeed, as opposed to the TO framework, in the HyTopS scheme for performing sensitivity analysis, we need

to find the velocity field¹, which is a challenging task. The velocity field needs to be defined in the HyTopS scheme due to changes in the location of microchannels during the shape optimization process. Second, because of having a simpler sensitivity analysis, the computational cost associated with performing sensitivity analysis in the TO scheme is smaller than the HyTopS method. Third, the solver in the suggested TO framework is the regular Finite Element Method (FEM) while the solver in the HyTopS method is IGFEM. FEM is much easier to implement in comparison with the IGFEM. It is worth noting that the main reason that the method of choice for the solver in the HyTopS method is IGFEM is its advantages against FEM for the Eulerian-based optimization schemes. Indeed, by projecting the domain over a stationary mesh in the IGFEM framework, similar to the other Eulerian approaches, the HyTopS optimization framework does not suffer from mesh distortion issues commonly encountered in the Lagrangian-based methods. Finally, the design space in the suggested TO method is larger than the HyTopS method due to the limitations stemming from the manufacturing constraints in the HyTopS approach as will be discussed in detail in Section 4.2.

The remainder of the manuscript is organized as follows: Section 2 presents the GRO thermal/hydraulic model and finite element discretization. We introduce the design optimization scheme and perform the sensitivity analysis in Section 3. Several numerical optimization problems using the proposed TO scheme are solved in Section 4.1. In Section 4.2, we solve a numerical example to compare the TO scheme, HyTopS optimization method, and SO approach. Finally, verification of the thermal model and the optimization results are presented in Section 5.

2 Physical model

In this study, we intend to perform a gradient-based topology optimization approach, which is an iterative process and requires many field evaluations. Thus, to reduce the computational burden, we need to take advantage of a GRO thermal/hydraulic model with acceptable accuracy. To this end, we present the key concepts and notations associated with the GRO model that we implemented in our design optimization framework.

To find the thermal and hydraulic responses of the microvascular composite, a two-dimensional domain is considered as shown in Fig. 1. The microvascular panel domain Ω is embedded with microchannels Γ_f and closure $\bar{\Omega}$ is bounded by $\partial\Omega = \bar{\Omega} - \Omega$. In terms of boundary conditions, the sides of the panel are insulated, and the inlet temperature,

¹In the IGFEM framework, the velocity field is defined as the partial derivative of the nodal coordinates with respect to the design variables.

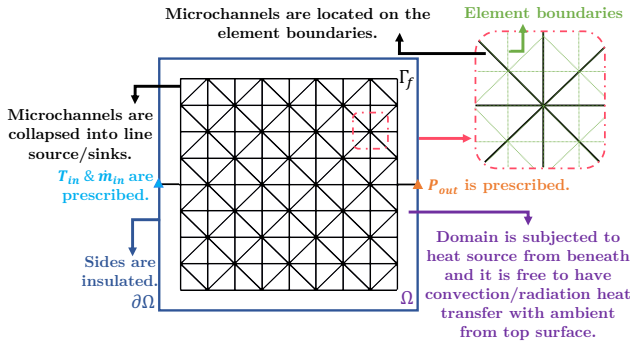


Fig. 1: Schematic of microvascular composite geometry and boundary conditions. The inset shows a portion of the conforming mesh.

inlet flow rate, and the outlet pressure of the microchannel network are prescribed.

The assumptions underlying the GRO thermal/hydraulic model are explained below. First and foremost, we collapse the microchannels into line source/sinks which can be justified by the small diameter to length ratio of microchannels. As a result, the microchannel wall temperatures become approximately equal to the fluid mixed-mean temperature. Second, the flow is assumed to be fully-developed, laminar, and steady-state. Third, the axial conduction of the coolant is assumed to be negligible in comparison with the axial advection. The justification of these assumptions is presented in Section 5.1.

Given the space of weight functions $\mathcal{V} = \{v \in H_0^1(\bar{\Omega})\}$ and the solution functions $\mathcal{T} = \{T \in H^1(\bar{\Omega}) : T_{in} = T_{in}^{ps}\}$, the weak form of the governing heat equation of the domain is given by: Find $T \in \mathcal{T}$ such that

$$\begin{aligned} & - \int_{\Omega} (\nabla v \cdot \mathcal{K} \nabla T + \tilde{h}v(T - T_{amb}) - vf) d\Omega \\ & - \sum_{j=1}^{n_{ch}} \int_{\Gamma_f^{(j)}} v \tilde{m}^{(j)} c_f \mathbf{t}^{(j)} \cdot \nabla T d\Gamma = 0, \quad \forall v \in \mathcal{V} \end{aligned} \quad (1)$$

where $\mathcal{K} = \kappa_p \mathbf{I}$ is the thermal conductivity tensor, κ_p is the thermal conductivity of the composite, T is temperature, T_{amb} is the ambient temperature, f is distributed heat source, n_{ch} is the number of microchannels, $\tilde{m}^{(j)}$ is the mass flow rate of microchannel j , $\mathbf{t}^{(j)}$ is the unit tangent row vector of the microchannel j in the flow direction, c_f is the coolant specific heat capacity, T_{in} is the temperature at the inlet of the microchannel network, T_{in}^{ps} is the prescribed value for the inlet temperature, and $\tilde{h} = h_{conv} + h_{rad}$ is the equivalent heat loss coefficient. h_{conv} and h_{rad} are the convection and radiation heat transfer coefficients, respectively. Note that the radiation heat transfer coefficient is estimated by linearizing the Stefan-Boltzmann law.

The Hagen-Poiseuille flow [43] method is used to determine the pressure drops and mass flow rates in the microchannel. The primary assumption in the Hagen-Poiseuille method is that the flow rate scales linearly with the pressure drop. In the first step, we can find the nodal pressures by solving the linear system of equations

$$\mathbb{G}\mathbb{P} = \mathbb{S}, \quad (2)$$

where \mathbb{G} is the assembled conductance matrix, \mathbb{P} is the column vector of nodal pressures, and \mathbb{S} is the column vector of external mass flow rates, respectively. \mathbb{G} , \mathbb{P} , and \mathbb{S} are assembled using the following equation for each microchannel (j),

$$g^{(j)} \begin{bmatrix} 1 & -1 \\ -1 & 1 \end{bmatrix} \begin{Bmatrix} P_{inlet}^{(j)} \\ P_{outlet}^{(j)} \end{Bmatrix} = \begin{Bmatrix} S_{inlet}^{(j)} \\ S_{outlet}^{(j)} \end{Bmatrix}, \quad (3)$$

where $g^{(j)} = CD^{(j)4}/\nu L^{(j)}$ is microchannel conductance, L is microchannel length, and D is microchannel diameter. C is equal to $\pi/128$ for a microchannel with circular cross-section [43,44]. $\nu = 0.0069 (T_{avg}^{ch}/273.15)^{-8.3}/\rho$ is the fluid kinematic viscosity, which is assumed to be temperature-dependent. ρ is the fluid density and $T_{avg}^{ch} = \frac{1}{|\Omega_f|} \int_{\Omega_f} T d\Omega_f$ is the average temperature of microchannels in Kelvin and $|\Omega_f|$ is the total volume of the microchannels [30]. Note that in this study, we assume that specific heat capacity, density, and thermal conductivity are temperature independent.

The computational domain is discretized by 3-node triangular finite elements. We place the microchannels on the boundaries of the elements as shown in Figure 1. The approximation of the temperature field in each element is given by

$$T_e^h(\mathbf{X}) = \sum_{i=1}^{n^e} N_i(\mathbf{X}) T_i = \mathbf{N}^e(\mathbf{X}) \mathbf{T}^e, \quad (4)$$

where \mathbf{X} is the spatial coordinates, n^e is the number of degree of freedoms (dof) in each element, $N_i(\mathbf{X})$ is the finite element shape functions, and T_i is the nodal dofs. \mathbf{N}^e is the row vector of shape functions for element (e) with dimension: $(1 \times n^e)$ and \mathbf{T}^e is the vector of nodal temperatures with dimension: $(n^e \times 1)$.

We can compute the thermal gradients by taking the derivative of (4) with respect to \mathbf{X} ,

$$\frac{\partial T_e^h(\mathbf{X})}{\partial \mathbf{X}} = \frac{\partial \mathbf{N}^e(\mathbf{X})}{\partial \mathbf{X}} \mathbf{T}^e = \mathbf{B}^e(\mathbf{X}) \mathbf{T}^e, \quad (5)$$

where $\mathbf{B}^e(\mathbf{X})$ is the partial derivative of $\mathbf{N}^e(\mathbf{X})$ with respect to \mathbf{X} with dimension: $(n^d \times n^e)$, where n^d is the dimension of the problem (in this study $n^d = 2$). Due to well-known stability issues for convection-dominated flow problems, we adopt the streamline-upwind Petrov-Galerkin (SUPG) technique [45] to stabilize the FEM and decrease the oscillations in the temperature field. In the SUPG method, we modify the weighing

function while maintaining equivalence to the original weak form. For further details regarding the implementation of SUPG function, readers are referred to our previous work in [40].

Implementation of the finite element method (FEM) results in the following system of equations:

$$\mathbb{K}\mathbb{T} = \mathbb{F}, \quad (6)$$

where \mathbb{K} is the global stiffness matrix, \mathbb{T} is the global nodal temperature vector, and \mathbb{F} represents the global nodal force vector.

As usual, \mathbb{K} is assembled from the element stiffness matrices \mathbf{K}^e ,

$$\begin{aligned} \mathbf{K}^e = & \int_{\Omega_e} \left(\mathbf{B}'^e(\mathbf{X}) \mathcal{H}(\mathbf{X}) \mathbf{B}^e(\mathbf{X}) + \mathbf{N}'^e(\mathbf{X}) \tilde{h} \mathbf{W}^e(\mathbf{X}) \right) d\Omega \\ & + \frac{1}{2} \sum_{j=1}^{n_{ch}} \int_{\Gamma_f^{(j)} \cap \partial\Omega_e} \mathbf{B}'^e(\mathbf{X}) \mathbf{t}^{(j)} \dot{m}^{(j)} c_f \mathbf{W}^e(\mathbf{X}) d\Gamma, \end{aligned} \quad (7)$$

where the prime symbol denotes the transpose, $\partial\Omega_e$ represents the boundary of element (e), \mathbf{W}^e is the SUPG weighting function defined as $\mathbf{W}^e = \mathbf{N}^e + \sum_{j=1}^{n_{ch}} \frac{\mathbf{t}^{(j)} \mathbf{B}^e}{\sum_{k=1}^{n_{ch}} |\mathbf{t}^{(j)} \cdot \nabla N_k|}$, where N_k is the shape function associated with node k . As mentioned earlier, the microchannels are located at the edges of elements. Since each edge is common between two adjacent elements, half of the microchannel flow rate is used in each one of those two elements to convect out the heat from them. This is the reason that the coefficient $1/2$ is written in the second term of (7).

The global nodal force vector \mathbb{F} in (6) is assembled from the element nodal force vector \mathbf{F}^e ,

$$\mathbf{F}^e = \int_{\Omega_e} \mathbf{W}'^e(\mathbf{X}) \left(f(\mathbf{X}) + \tilde{h} T_{amb} \right) d\Omega. \quad (8)$$

We use standard isoparametric elements with Gauss quadrature to calculate the integrals that define element stiffness matrices and load vectors. Note that the GRO model presented in this section is validated and verified in previous studies for the IGFEM framework [2, 3, 38, 40, 42, 46, 47]. In this study, we verify our GRO-FEM thermal solver by using ANSYS/FLUENT in Section 5.1.

3 Gradient-based topology optimization scheme

A topology optimization problem can be formulated as

$$\begin{aligned} & \min_{\boldsymbol{\alpha}} \theta(\mathbb{T}(\mathbf{X}, \boldsymbol{\alpha}), \mathbf{X}, \boldsymbol{\alpha}), \\ \text{such that : } & 0 \leq \alpha_i \leq 1, \\ & \mathbf{g}(\mathbb{T}(\mathbf{X}, \boldsymbol{\alpha}), \mathbf{X}, \boldsymbol{\alpha}) \leq \mathbf{0}, \\ \text{and } & \mathbb{K}\mathbb{T} = \mathbb{F}, \end{aligned} \quad (9)$$

where θ is the objective function, $\boldsymbol{\alpha}$ is the vector of design parameters, and \mathbf{g} is the vector of inequality constraints. In

this study, the objective is to minimize the maximum temperature of the panel with pressure drop and volume fraction constraints. However, considering that the max-operator is not differentiable, T_{max} is approximated by a differentiable alternative, namely a p -mean temperature $\|T\|_p = \left(\frac{1}{|\Omega|} \int_{\Omega} T^p d\Omega \right)^{1/p}$ where $|\Omega|$ is the area of the domain.

Inspired by the Solid Isotropic Material with Penalization (SIMP) method, we define a set of design variables ($\boldsymbol{\alpha}$), which act analogously as the design variables in the SIMP method. Using this set of design variables, we can penalize the diameters of the microchannels by defining an effective diameter

$$D_{eff}^{(i)} = D_{min} + \alpha_i^\eta (D_{max,i} - D_{min}), \quad (10)$$

where η is the penalization power, D_{min} is the minimum diameter that we consider for the microchannels to prevent numerical issues, and $D_{max,i}$ is the maximum diameter of the microchannel (i). η is introduced to penalize intermediate diameters and push them toward either zero or the maximum value. In this study, we use the continuation method based on the work presented in [48] to start with a more convex problem and gradually push towards less convex, thereby promoting better local optima. In the continuation method, we start the optimization process with a low penalization value ($\eta = 1$), let the procedure converge, then increase η with 0.5, again let the algorithm converge, and continuing this pattern until η equals 3.

Collapsing the microchannels into line source/sinks allows for placing the microchannels exactly on the boundaries of the elements. Note that the same idea has been used in truss topology optimization [49, 50]. During the TO process, the diameters of microchannels are optimized and the microchannels with flow rates below a prescribed threshold are viewed as unnecessary and are subsequently removed from the network design.

Applying the mass flow rate threshold to remove the microchannels with low flow rates may result in non-consistent diameter changes for microchannel connections, as schematically shown in Fig. 2. This issue mainly occurs when we select a relatively large mass flow rate threshold. This change in diameter of adjacent microchannels results in a non-optimal solution. To alleviate this issue, we propose the following methodology. After performing the continuation method and obtaining the optimized solution, we omit the design variables associated with the removed microchannels from the design space. Then in this new design space, we perform the optimization process with $\eta = 3$ by starting from the optimized solution of the continuation method. This optimization process allows the optimizer to adjust the diameters of adjacent microchannels to almost the same value (See Fig. 2(c)). Note that this last step may need to be repeated several times since the flow rate in the new microchannels may go below

the prescribed mass flow rate threshold. However, we experience the design variables rather go in the opposite direction since the remaining microchannels have to carry flow rates that earlier were carried by the removed microchannels.

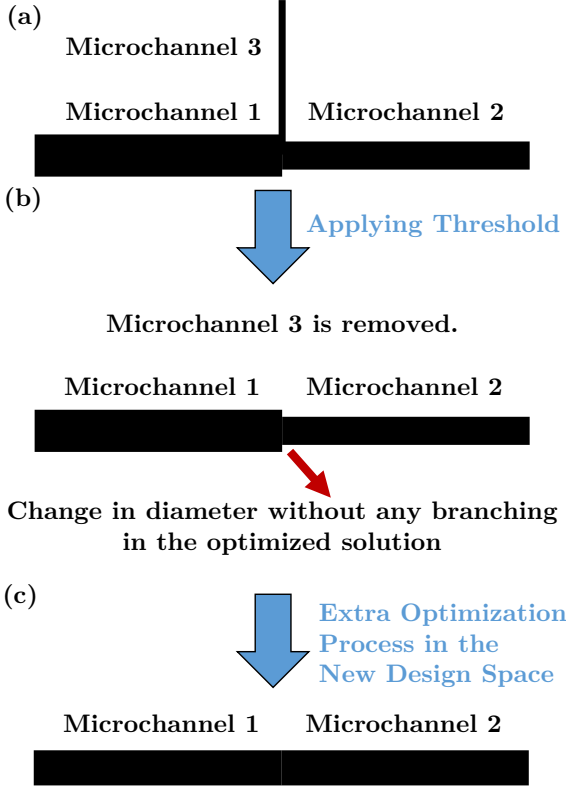


Fig. 2: (a) The schematic of microchannels 1, 2, and 3 before applying mass flow rate threshold. (b) After applying the threshold, microchannel 3 is removed. Now, there is a change in diameter between microchannel 1 and 2, which results in a non-optimal solution. (c) Performing an extra optimization process in a new design space, in which we omit the design variable associated with the removed microchannels from the design space. The optimizer adjusts the diameter of microchannels 1 and 2 to almost the same value.

The sensitivity of the objective function with respect to the design variables α_i is obtained using the adjoint sensitivity method. Differentiating the objective function $\theta = \left(\frac{1}{|\Omega|} \int_{\Omega} (\mathbb{N}\mathbb{T})^p d\Omega\right)^{1/p}$ with respect to the design variables α_i yields:

$$\frac{d\theta}{d\alpha_i} = \left(\frac{\partial\theta}{\partial\mathbb{T}}\right)' \frac{\partial\mathbb{T}}{\partial\alpha_i} + \frac{\partial\theta}{\partial\alpha_i}, \quad (11)$$

where $\partial\theta/\partial\mathbb{T}$ and $\partial\theta/\partial\alpha_i$ can explicitly be found, and the only unknown is temperature sensitivity $\partial\mathbb{T}/\partial\alpha_i$.

In the adjoint method, instead of finding $\partial\mathbb{T}/\partial\alpha_i$, we annihilate it from (11). To do so, we add zero to (11), i.e. we write

$$\frac{d\theta}{d\alpha_i} = \left(\frac{\partial\theta}{\partial\mathbb{T}}\right)' \frac{\partial\mathbb{T}}{\partial\alpha_i} + \frac{\partial\theta}{\partial\alpha_i} + \lambda' \left(-\mathbb{K} \frac{\partial\mathbb{T}}{\partial\alpha_i} + \mathbb{F}_{pseudo}^i\right), \quad (12)$$

where λ is the arbitrary adjoint variable. The zero added to (11) is actually the pseudo problems ($\mathbb{K} \frac{\partial\mathbb{T}}{\partial\alpha_i} = \mathbb{F}_{pseudo}^i$), which are obtained by differentiating the primal problem (6) with respect to each one of the design variables α_i . Note that the pseudo force is $\mathbb{F}_{pseudo}^i = -\frac{\partial\mathbb{K}}{\partial\alpha_i}\mathbb{T} + \frac{\partial\mathbb{F}}{\partial\alpha_i}$.

By rearranging the terms in (12), we have

$$\frac{d\theta}{d\alpha_i} = \left(\left(\frac{\partial\theta}{\partial\mathbb{T}}\right)' - \lambda' \mathbb{K}\right) \left(\frac{\partial\mathbb{T}}{\partial\alpha_i}\right) + \frac{\partial\theta}{\partial\alpha_i} + \lambda' \left(-\frac{\partial\mathbb{K}}{\partial\alpha_i}\mathbb{T} + \frac{\partial\mathbb{F}}{\partial\alpha_i}\right). \quad (13)$$

The adjoint response λ in (13) may be selected arbitrarily such that it makes the coefficient of $\partial\mathbb{T}/\partial\alpha_i$ zero:

$$\mathbb{K}' \lambda = \frac{\partial\theta}{\partial\mathbb{T}}. \quad (14)$$

Thus, λ can be obtained by solving (14).

Note that in (13), $\partial\theta/\partial\alpha_i = 0$, since the objective function considered in this study is not explicitly function of α and $\partial\mathbb{F}/\partial\alpha_i$ is also zero. Therefore, we obtain the gradient of the objective function with respect to α_i by

$$\frac{d\theta}{d\alpha_i} = \lambda' \left(-\frac{\partial\mathbb{K}}{\partial\alpha_i}\mathbb{T}\right), \quad (15)$$

where $\partial\mathbb{K}/\partial\alpha_i$ can be obtained by assembling the element quantity $\partial\mathbf{K}^e/\partial\alpha_i$:

$$\frac{\partial\mathbf{K}^e}{\partial\alpha_i} = \frac{1}{2} \sum_{j=1}^{n_{ch}} \int_{\Gamma_f^{(j)} \cap \partial\Omega_e} \mathbf{B}^{e'} \mathbf{t}^{(j)} \frac{\partial \dot{m}^{(j)}}{\partial\alpha_i} c_f \mathbf{W}^e d\Gamma. \quad (16)$$

We compute $\partial \dot{m}^{(j)}/\partial\alpha_i$ and $\partial\mathbf{P}/\partial\alpha_i$ in (16) as

$$\begin{aligned} \frac{\partial \dot{m}^{(j)}}{\partial\alpha_i} &= \frac{\partial g^{(j)}}{\partial\alpha_i} |(P_{inlet}^{(j)} - P_{outlet}^{(j)})| \\ &+ g^{(j)} \text{sign}(P_{inlet}^{(j)} - P_{outlet}^{(j)}) \left(\frac{\partial P_{inlet}^{(j)}}{\partial\alpha_i} - \frac{\partial P_{outlet}^{(j)}}{\partial\alpha_i}\right), \end{aligned} \quad (17)$$

and

$$\frac{\partial\mathbf{P}}{\partial\alpha_i} = \mathbb{G}^{-1} \left(-\frac{\partial\mathbb{G}}{\partial\alpha_i}\mathbf{P}\right), \quad (18)$$

respectively. Note that $\partial\mathbb{G}/\partial\alpha_i$ can be explicitly evaluated.

In summary, to perform the adjoint sensitivity analysis, we obtain λ from (14) and by substituting it into (15), we evaluate the gradient of the objective function with respect to α_i . The FMINCON SQP algorithm available in MATLAB [51] is used to solve the optimization problems. The algorithm associated with performing the optimization process explained in Section 3 is shown in Fig. 3.

Algorithm

- 1: **for** $\eta = 1, 1.5, 2, 2.5$, and 3 , **do**
 - 2: Compute D_{eff} via (10) and perform hydraulic and thermal analysis via (2) and (6)
 - 3: Perform adjoint sensitivity analysis via (15)
 - 4: Update design variables and repeat Steps 2-4 until convergence
 - 5: In case of non-consistent diameter changes in microchannel after applying mass flow rate threshold, **do**
 - 6: Omit the design variables associated with the removed microchannels of the optimized solution of Steps 1-4 from the design space
 - 7: Perform extra optimization process starting from the optimized solution of steps 1-4 with $\eta = 3$ and repeat this step until removing the non-consistency in diameter changes
-

Fig. 3: The algorithm that summarizes the steps explained in Section 3.

4 Numerical examples

We solve two sets of optimization problems to examine the capability of the proposed methodology for designing actively-cooled microvascular composites. In the first set of problems, we test the optimization algorithm for designing a microvascular composite subjected to uniform and concentrated heat fluxes. In the second set of problems, we compare the optimized solutions obtained from the proposed TO scheme with the HyTopS optimization method and SO approach based on several quality assessment measures.

4.1 Problem set 1: Topology optimization

The schematic of the problem is presented in Fig. 4. A thin carbon-fiber/epoxy matrix composite panel with embedded microchannels is subjected to heat flux from beneath and has convection and radiation heat transfer with the ambient from the top surface. The adiabatic boundary condition is considered for the sides of the panel. The coolant is assumed to be 50:50 water:ethylene glycol mixture, which enters the network from the left inlet with a volumetric flow rate of 22.5 mL min^{-1} and temperature of 20°C . The coolant exits the network from the right outlet at a zero-reference pressure. The microchannel cross-sections are assumed to be circular with a maximum diameter of $450 \mu\text{m}$. The material properties and simulation parameters are listed in Table 1.

The optimization problem is to find the optimized design for the cooling network, which minimizes the p -mean ($p=10$) temperature of the microvascular composite panel. The reason for selecting this value is discussed in Appendix A. The optimization problem is subjected to a maximum network pressure drop constraint of 40 KPa and a maximum void volume fraction of 0.005 . The void volume fraction is defined as the ratio of total microchannel volume over the total volume of the composite panel, i.e., $f_{void} = \frac{\sum_{i=1}^{n_{ch}} V^{(i)}}{V_{panel}}$. The design variables are α_i associated with each microchannel (i). In total, 210 design variables are considered for this problem.

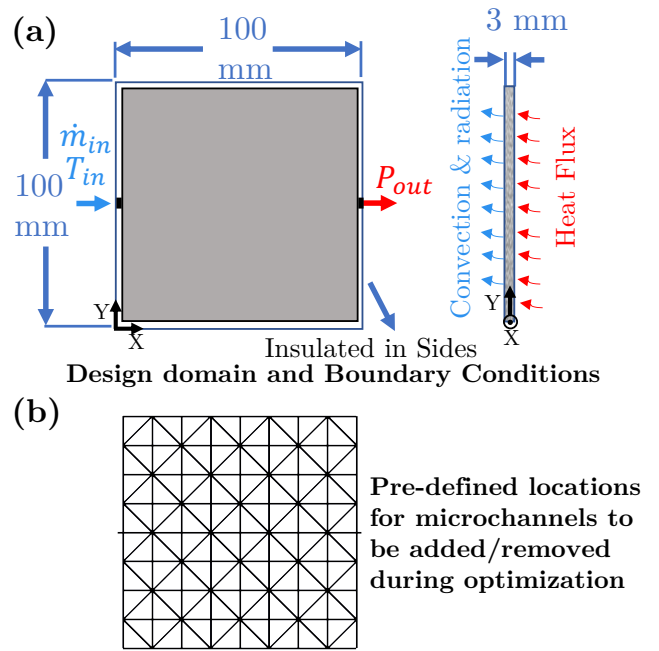


Fig. 4: (a) Problem setup and (b) pre-defined locations for the microchannels to be added or removed during the optimization process.

Table 1: Simulation parameters.

Length and width of panel (mm)	100
Thickness, t (mm)	3
Composite thermal conductivity, κ_p ($\text{W m}^{-1} \text{K}^{-1}$)	2
Composite density, ρ_c (kg m^{-3})	1430
Ambient Temperature, T_{amb} ($^\circ\text{C}$)	22
Convection coefficient, h_{conv} ($\text{W m}^{-2} \text{K}^{-1}$)	18
Emissivity, ϵ	0.95
Coolant inlet temperature, T_{in} ($^\circ\text{C}$)	20
Coolant inlet flow rate, \dot{V}_{in} (mL min^{-1})	22.5
Coolant conductivity, κ_c ($\text{W m}^{-1} \text{K}^{-1}$)	0.419
Coolant heat capacity, c_f ($\text{J kg}^{-1} \text{K}^{-1}$)	3494
Coolant density, ρ_c (kg m^{-3})	1065

The pre-defined locations of the microchannels are shown in Fig. 4 (b). As discussed in Section 3, we use the continuation method to obtain the optimized solution in which we increase the penalization power from 1 to 3 using 0.5 intervals. Moreover, the minimum diameter in (10) is set to $60 \mu\text{m}$ and the reason for that is discussed in Appendix B. The mass flow-rate threshold below which microchannels are removed after optimization is 0.003 gr/s . The panel is assumed to be subjected to a uniform heat flux of 500 Wm^{-2} .

The optimization problem is first solved by starting the optimization process from a 2-branch horizontal parallel network as shown in Fig. 5 (a). Using the proposed TO method, the optimized solution is obtained as shown in Fig. 5 (b). Through the optimization process, the p -mean temperature of the panel is reduced from 29.4°C to 22.9°C and the maximum temperature of the panel is decreased from 33.5°C to 25.3°C . The value of the p -mean temperature at the end of the continuation method by considering $\eta = 1$ is 23°C , and it remains at 22.9°C for the optimized solutions obtained in the rest of the continuation method. Note that all of the temperatures that we are presenting in this study are the temperatures after removing the microchannels with the mass flow rates lower than the prescribed threshold. As it is discussed in Appendix C, we selected the mass flow rate threshold in such a way that the effect of removing the microchannels with mass flow rates lower than that threshold on the p -mean temperature of the domain is negligible. The flow rate distribution for the initial and optimized designs are depicted in Fig. 5 (c) and (d), respectively. The arrows in Fig. 5 (c) and (d) indicate the flow directions along the microchannels. We refer to this optimization problem as ‘‘UHF1’’, which is an abbreviation for uniform heat flux 1.

To test the optimality, we solve the same optimization problem by starting from two other initial designs far from the expected optimized solution obtained in UHF1 (compare Fig. 5 (g) and (m) with (b)). These optimization problems are named ‘‘UHF2’’ and ‘‘UHF3’’. For UHF2, the optimized solution obtained from topology optimization satisfies the constraints, but also it reduced the p -mean temperature of the domain from 27.4°C to 22.8°C and decreased the maximum temperature of the panel from 32.3°C to 25.3°C (see Fig. 5 (k) and (l)). The p -mean temperature at the end of each step of the continuation method by considering $\eta = 1$ to 3 is 22.8°C . Note that for the reference design of UHF3, we considered a uniform design with diameters equal to 50% of the maximum diameter considered in this study. This reference design satisfies the volume fraction constraint, but it does not satisfy the pressure drop constraints.² The optimized solution obtained from UHF3 satisfies both the volume fraction and pressure constraints, but satisfying these constraints comes at the price

of slightly rising the p -mean temperature of the panel from 22.4°C to 22.8°C . It also leads to an increase in the maximum temperature of the domain from 24.7°C to 25.2°C (see Fig. 5 (q) and (r)). Note that the p -mean temperature at the end of the continuation method by considering $\eta = 1$ and 1.5 are 23°C and it remains at 22.8°C for the optimized solution of $\eta = 2$ to 3.

The history plots associated with the optimization problems UHF1 and UHF2 are shown in Fig. 5 (s and t). The sudden peaks in the history plots are due to using the continuation method for solving the optimization problems in this study. The markers in the history plots corresponds to the end of each step of the continuation method. Note that the optimization framework reached three different local minima as shown in Figure 5 (b), (h) and (n) with relatively close objective values (22.90°C for UHF1, 22.82°C for UHF2, and 22.83°C for UHF3). Note that the objective values of the optimized designs before removing the microchannels with mass flow rates lower than the prescribed threshold were also very close to the values obtained after removing those microchannels as it is also discussed in Appendix C. The objective values before removing the low flow rate microchannels were 22.95°C for UHF1, 22.89°C for UHF2, and 22.89°C for UHF3.

The designs obtained in optimization problems UHF1-UHF3 are based on the pre-defined 8 by 8 structure considered for microchannels as shown in Fig. 4 (b). To investigate the effect of this pre-defined structure on the optimization problem, we repeat the UHF3 problem by considering 6 by 6 and 12 by 12 initial network structures. Note that there are 122, 210, and 458 design parameters in the optimization problems for 6 by 6, 8 by 8, and 12 by 12 initial network structures, respectively. The results are shown in Fig. 6. As illustrated in the figure, the difference in the p -mean temperature of the optimized solutions is only about 1% and the optimized designs follow similar general patterns.

To further investigate the capability of our proposed method, we solve the same optimization problem for two cases that have concentrated heat fluxes as shown in Fig. 7 (a and h). In these two cases, in addition to the uniform heat flux of 500 Wm^{-2} , the panel is subjected to two concentrated heat fluxes of 5000 Wm^{-2} . We use the abbreviations CHF1 (Concentrated Heat Flux 1) and CHF2 (Concentrated Heat Flux 2) to refer to the optimization problems with the heat fluxes shown in Fig. 7 (a) and (h), respectively. Our expectation in these two cases is to observe that the optimizer increases the number of microchannels and their flow rate shares on the locations where the concentrated heat fluxes are introduced to effectively convect out the enormous amount of heat generated on those particular locations. Based on the same analysis as discussed in Appendix B, in this problem, we set the minimum diameter used in (10) to $40 \mu\text{m}$. The results of CHF1 and CHF2 are shown in Fig. 7. As it was expected,

²Note that for this problem, it is not possible to have a uniform design which simultaneously satisfies both the volume fraction and pressure drop constraints.

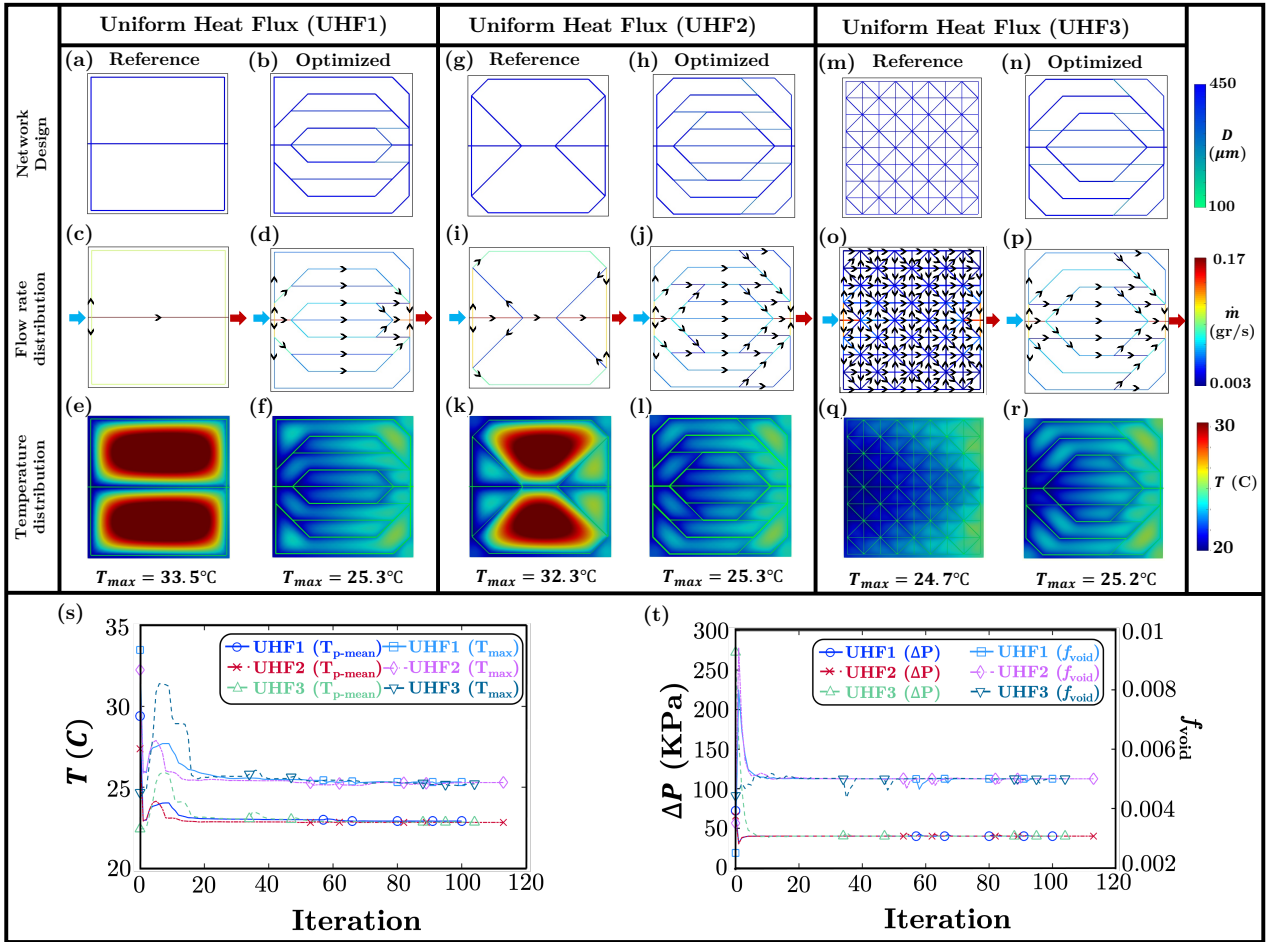


Fig. 5: (a, b) Microchannel networks, (c, d) flow rate distributions, and (e, f) temperature distributions for reference and optimized designs of UHF1. (g, h) Microchannel networks, (i, j) flow rate distributions, and (k, l) temperature distributions of initial and optimized designs of UHF2. (m, n) Network design, (o, p) flow rate distributions, and (q, r) temperature distributions for reference and optimized designs of UHF3. The evolution of (s) the objective function and (t) inequality constraints for both UHF1, UHF2, and UHF3. The optimization problems are subjected to constraints on the maximum void volume fraction and maximum pressure drops ($f_{void} \leq 0.005$ and $\Delta P \leq 40$). The markers in the history plots correspond to the end of each step of the continuation method (0.5 increase in the η value).

in the optimized solutions obtained from CHF1 and CHF2, the optimizer increased the number of microchannels in the neighborhood of the concentrated heat flux locations (See Fig. 7 (c, j)). Through the optimization process, the p -mean temperature of the panel is reduced from 53.1°C to 24.5°C in CHF1 and from 39.2°C to 25.0°C in CHF2. Moreover, the maximum temperature of the panel is reduced by $\sim 59\%$ in CHF1 (76.1°C to 30.9°C) and $\sim 43\%$ in CHF2 (57.1°C to 32.6°C). Figure 7 (o and p) show the history plots of CHF1 and CHF2.

Note that the optimized solutions obtained in this section are symmetric with respect to the centerline, as expected. It is worth pointing out that we have not imposed any symmetric boundary conditions on the problem and the physic

itself dictates the symmetric optimized topology. Producing symmetric design for these problems can be attributed to the accuracy of our analytical sensitivity analysis. Note that we have also confirmed the accuracy of our sensitivity analysis against the finite difference method (see Appendix D).

4.2 Problem set 2: TO vs HyTopS vs SO

In this section, we aim to compare the TO scheme with HyTopS and SO methods for actively-cooled microvascular composites. The problem setup, material properties, and simulation parameters are the same as the problem UHF1 solved in Section 4.1, except the inlet of the network is located at

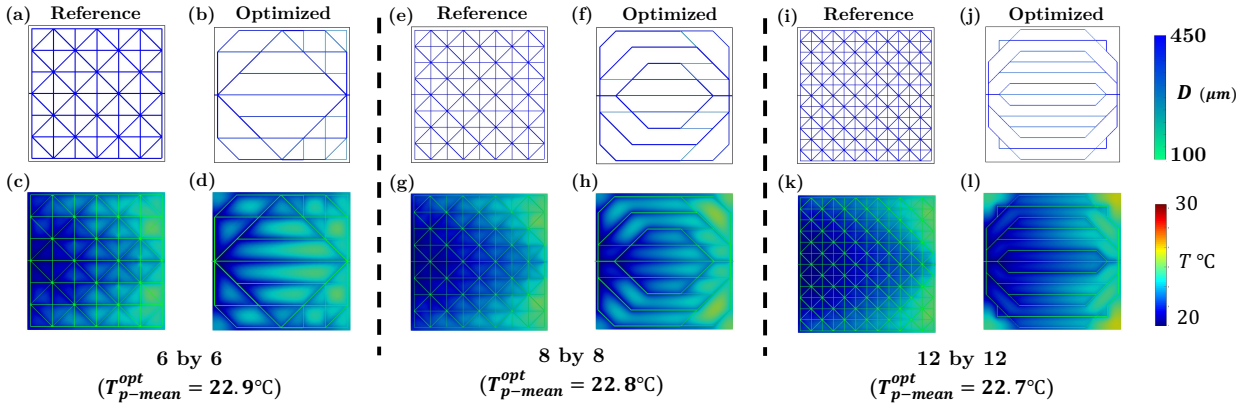


Fig. 6: Microchannel networks and temperature distributions for reference and optimized designs of UHF3 optimization problem by considering (a-d) 6 by 6, (e-h) 8 by 8, and (i-l) 12 by 12 initial network structures. The optimization problems are subjected to constraints on the maximum void volume fraction and maximum pressure drop ($f_{void} \leq 0.005$ and $\Delta P \leq 40$). Note that the change in the p -mean temperature of the optimized solution is about 1%.

the top left corner, and the outlet is at the right bottom corner. The objective function is to minimize the p -mean temperature ($p = 10$) of the panel. Two inequality constraints on the maximum void volume fraction ($f_{void} < 0.004$), and the maximum network pressure drop ($\Delta P < 85$ KPa) are imposed on the optimization problem.

For the reasons explained in the Introduction, our method of choice for HyTopS and SO schemes is IGFEM. We impose 77 and 21 geometrical constraints for HyTopS and SO, respectively. These geometrical constraints are schematically shown in Fig. 8. The main goal of these constraints is preventing the microchannels from self-crossing. To this end, a set of triangles are constructed as shown in Fig. 8 (a). Let γ_i represent the interior angles (computed counterclockwise) and A_j denotes the area of the triangles. The geometrical constraints are defined as: (i) $\sin(\gamma_i) > \sin(\gamma_{min})$ and (ii) $A_j > A_{min}$, where γ_{min} and A_{min} are the minimum interior angle and area of triangles considered by the designer. The second condition is mathematically redundant, however, numerically it is required. Indeed, when the end points of the microchannels get very close to each other, the computation of $\sin(\gamma_i)$ gets inaccurate and the second condition helps in preventing the self-crossing. For the HyTopS and SO methods, we set $\gamma_{min} = 0.087$ radian and $A_{min} = 0.001A_p$, where A_p is the surface area of the panel. For further details regarding these geometrical constraints, readers are referred to [3].

The design parameters in the TO scheme are only the weighting parameters (α_i). For the HyTopS method, in addition to the weighting parameters (α_i), the location of the end points of the microchannels are design parameters. Finally, for the SO approach, the design parameters are diameters and the location of the end points of the microchannels. In

total, 210, 63, and 19 design parameters are defined for TO, HyTopS, and SO methods, respectively.

The reference design is a 2-branch parallel horizontal network with a maximum temperature of 33.5°C as shown in Fig. 9 (a) and (c). Fig. 9 (d), (g), and (j) represent the optimized solutions obtained from TO, HyTopS, and SO schemes, respectively. To effectively compare the optimized solutions obtained from these schemes, we consider several crucial design factors such as: (i) maximum temperature and p -mean temperature, (ii) network redundancy, (iii) manufacturability, and (iv) temperature uniformity.

In terms of maximum temperature, the SO approach by altering the shape of the microchannel network decreased the maximum temperature from 33.5°C in the reference design to 29.5°C in the optimized solution. As it was expected, the TO and HyTopS methods outperform the SO scheme by taking advantage of topological changes. TO and HyTopS reduced the maximum temperature of the initial design by 25.1% and 23.3%, respectively. (TO: (from 33.5°C to 25.1°C) and HyTopS: (from 33.5°C to 25.7°C)). The same pattern can be seen in the p -mean temperature of the panel. The p -mean temperature of the panel is 29.3°C in the reference design. The SO, HyTopS, and TO methods reduced the p -mean temperature of the panel to 25.5°C , 23.1°C , and 22.8°C , respectively.

The other crucial design factor is network redundancy, which is of great importance in both providing temperature uniformity and also in circumventing the possible microchannel blockage. The small size of microchannels makes them highly susceptible to blockage from the damage in the network or presence of particles in the fluid. Living organisms such as plant leaves or human cardiovascular systems take advantage of network redundancy to survive under damage

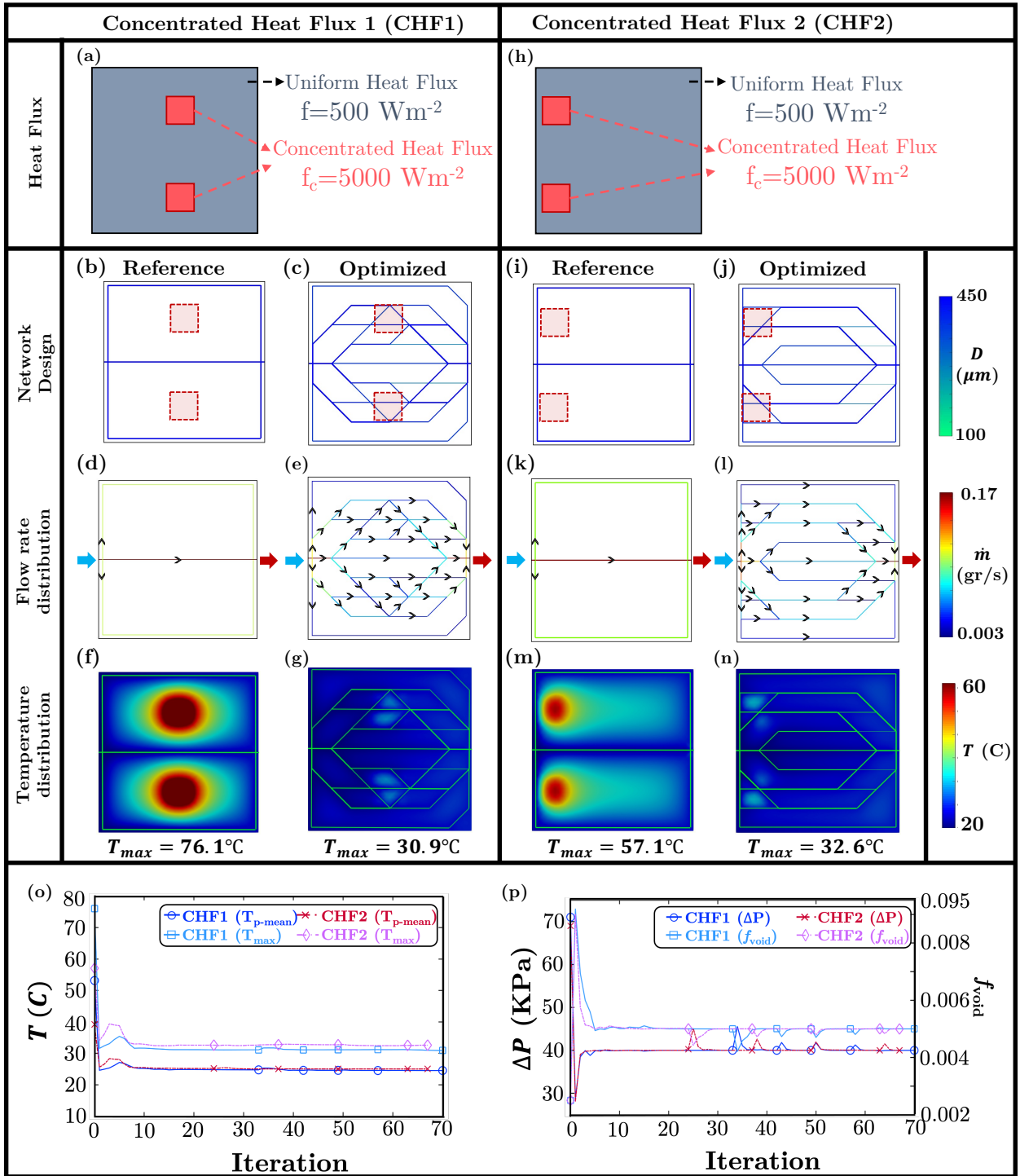


Fig. 7: (a) Heat flux distribution, (b, c) design of microchannel networks, distribution of (d, e) flow rate, and (f, g) temperature for reference and optimized designs of CHF1. (h) Distribution of heat flux, (i, j) microchannel networks, (k, l) flow rate distributions, and (m, n) temperature distributions of initial and optimized designs of CHF2. History plot of (o) the objective function and (p) constraints for both CHF1 and CHF2. The optimization problems are subjected to a constraint on the maximum void volume fraction and maximum pressure drops ($f_{void} \leq 0.005$ and $\Delta P \leq 40$ KPa). Note that for CHF1, the p -mean temperature value is 24.8°C at the end of continuation method with $\eta = 1$, and then remains at 24.5°C for the optimized solution of the next steps of the continuation method. For the CHF2, the p -mean temperature is 25.2°C at the end of the first step of the continuation method, and then stays at 25°C for the optimized solution of the next steps.

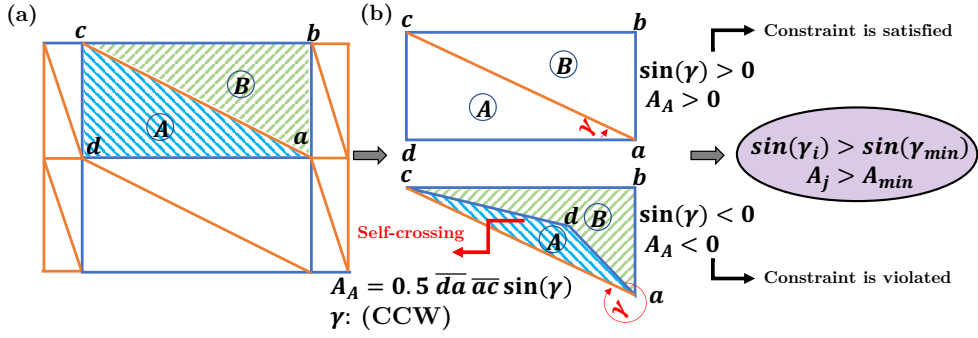


Fig. 8: (a) Triangles introduced to help preventing self-intersections as explained in Section 4.2. (b) A set of nonlinear inequality constraints are defined to aid preventing the self-crossing. Examples where nonlinear geometrical constraint is violated and satisfied are provided.

or blockage of vascular channels. We performed extensive studies on the importance of network redundancy for designing blockage-tolerant cooling networks in our previous studies [42, 52]. The optimized solution of TO possess more microchannels and branchings than the optimized designs of HyTopS and SO. Obviously, due to the redundancy in the number of microchannels, TO can handle microchannel blockage in a better way than the SO and HyTopS solutions.

One of the good features of the TO design is that the angles between the microchannels are either 45° or 90° . This feature would not allow the microchannels to be very close to each other, which may lead to issues such as leakage in the microchannel network. As it was mentioned earlier, for the HyTopS and SO schemes, we need to impose a set of manufacturing constraints to prevent the microchannels from getting too close to each other. Imposing these constraints on the optimization problem limits the design space.

Temperature uniformity is one of the key design factors for cooling networks. However, having a uniform temperature is effective when it is accompanied by low average temperature. We plot the probability density function (PDF) of the nodal panel temperature in Fig. 10, and also we report the average and the standard deviation (STD) of the panel temperatures in Table 2 to compare the optimized solutions in terms of temperature uniformity. To compute PDF, we used *ksdensity* function in MATLAB, in which PDF is defined as $\hat{f}(T) = \frac{1}{nh} \sum_{j=1}^n K((T - T_j)/h)$, where h is the bandwidth, T is the temperature, n is the number of data points, and $K(\cdot)$ is the kernel smoothing function. The optimized solution of the TO scheme demonstrates a higher temperature uniformity with a lower average temperature in comparison with the solutions of SO and HyTopS methods.

To further investigate this matter, we solve another optimization problem using the TO and HyTopS schemes by considering the variance of nodal temperatures as the objective function. The variance of nodal temperatures can be deemed

Table 2: Comparison between the results obtained from TO, HyTopS, and SO methods for the Problem solved in Fig. 9.

Measures	TO	HyTopS	SO
$T_{p-mean}(^{\circ}C)$	22.8	23.1	25.5
$T_{max}(^{\circ}C)$	25.1	25.7	29.5
$T_{avg}(^{\circ}C)$	22.5	22.6	24.1
$STD(T)(^{\circ}C)$	1.2	1.3	2.3

as a measure of temperature uniformity. We define this objective function as $\sigma^2(T) = \frac{1}{|\Omega|} (\int_{\Omega} (T - \|T\|_1)^2 d\Omega)$. This equation can be simplified to $\sigma^2(T) = (\|T\|_2)^2 - (\|T\|_1)^2$. Thus, we can use the same sensitivity analysis that we developed in this study for this objective function. We consider the same inequality constraints on the maximum network pressure drop as the optimization problem solved in Fig. 9, i.e., $\Delta P < 85$ KPa. We set the maximum allowable volume fraction constraint to 0.0045. This value is slightly higher than the value that we considered in the optimization problem solved in Fig. 9 to give the optimizer more flexibility in providing network redundancy and temperature uniformity.

We start the optimization process from a single branch network with a variance of 36.5 and an average temperature of $30.4^{\circ}C$. The designs obtained from the TO and HyTopS schemes are shown in Fig. 11(d) and (g), respectively. The design obtained from the TO approach is quite interesting as it is similar to the general pattern that we observe in the human cardiovascular systems with veins and capillaries. The variance of surface temperature in the optimized design of the TO scheme is 0.765 and for the optimized design of the HyTopS method is 1.01 as it is shown in Fig. 11 (f) and (i), respectively. Moreover, the average temperature of the optimized design of the TO scheme is slightly lower than the optimized network of the HyTopS method ($22.4^{\circ}C$ for TO vs $22.6^{\circ}C$ for HyTopS). Hence, we can conclude that the TO

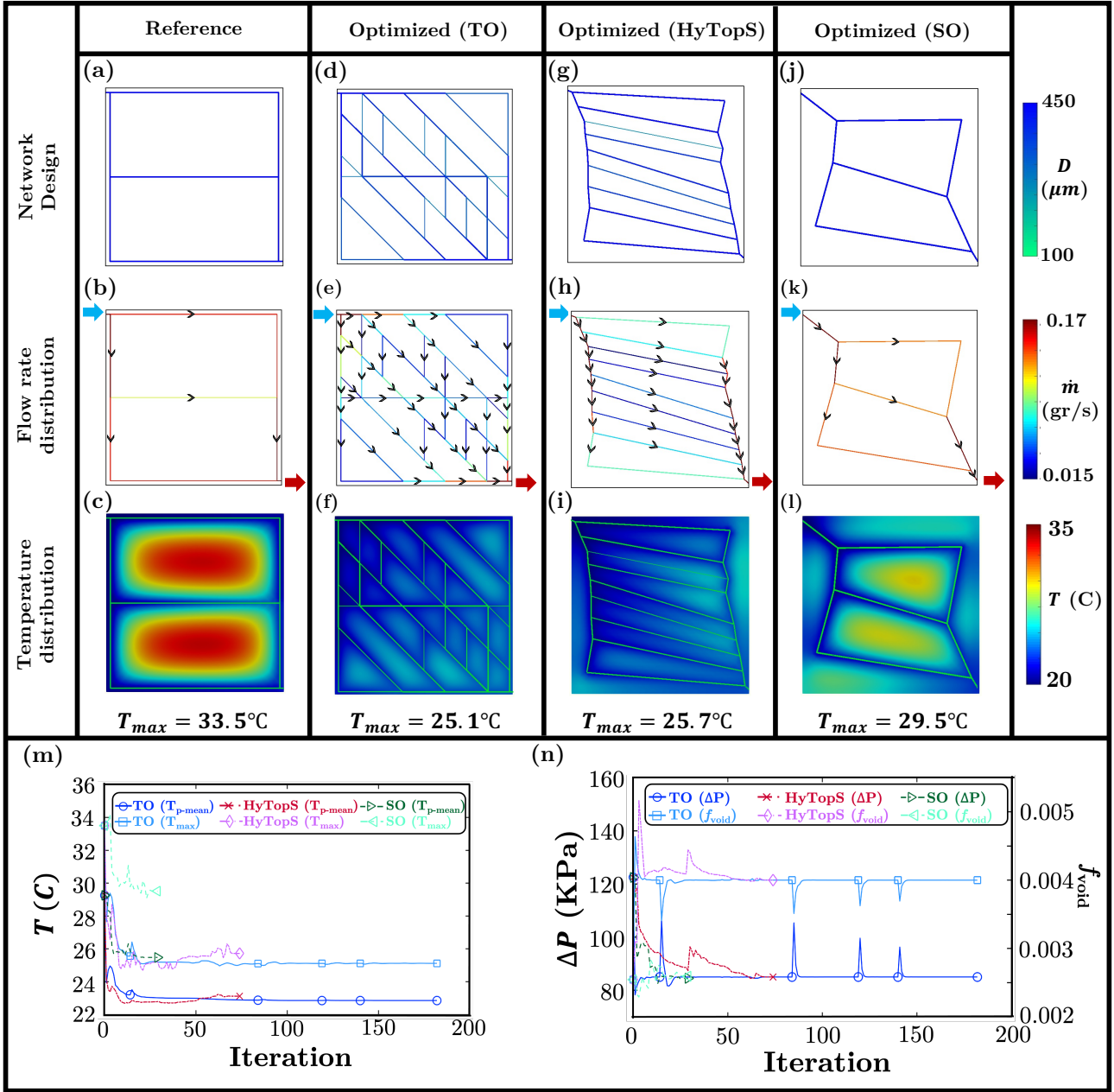


Fig. 9: (a) Reference design and its respective (b) flow rate and (c) temperature distributions. Optimized design, flow rate and temperature distributions obtained from (d, e, f) TO, (g, h, i) HyTopS, and (j, k, l) SO schemes for the optimization problem of Section 4.2 using p -mean temperature of the panel as the objective function. History plots of (m) the objective function and maximum temperature and (n) the pressure drop and volume fraction constraints. Note: The optimization problem is subjected to a maximum pressure drop constraint of 85 KPa and maximum void volume fraction of 0.004. Note that for the TO method, the p -mean temperature value is 23.2°C at the end of the continuation method with $\eta = 1$, and then remains at 22.8°C for the optimized solution of the next steps of the continuation method.

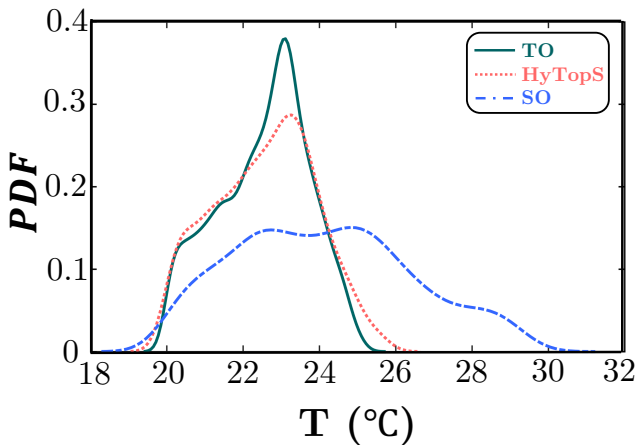


Fig. 10: Probability density function (PDF) of nodal temperatures of the optimized solutions obtained in the optimization problem solved in Fig. 9 using TO, HyTopS, and SO schemes.

optimization scheme outperforms the HyTopS method based on producing a more uniform temperature distribution with a lower average temperature.

The optimized solution of TO scheme after using the continuation method is shown in Fig. 12 (a). As it is indicated by the red circle in the figure, we can observe non-consistent diameter changes for microchannel connections in two locations. After applying the additional optimization process explained in Section 3 and Fig. 2, these non-consistencies are removed as shown in Fig. 12 (b). Note that the objective value in the optimized solution of the continuation method, before removing the low flow rate microchannels was 0.761. After applying the mass flow rate threshold, the objective value increased to 0.767. This small rise is expected since we removed the low flow rate microchannels. We know at this stage that the remaining microchannels have to carry flow rates that earlier were carried by the removed microchannels. By using the additional optimization step, we allow the optimizer to optimize the distribution of the flow rate in the new design space for the purpose of minimizing the objective function (variance of surface temperature). We observed that the objective value decreases to 0.765 after using the additional optimization step.

Finally, it is also worth mentioning that the computational cost associated with performing the sensitivity analysis in the TO scheme is smaller in comparison with the SO and HyTopS methods. One of the main reasons for that is the essence of finding the partial derivative of the nodal coordinates with respect to the design variables, the so-called velocity field, in the Eulerian-based shape optimization schemes such as HyTopS and SO methods used in this study. The velocity field is required to be computed in the SO and HyTopS schemes because of the changes in the location of microchannels

during the shape optimization process. Readers are referred to [40] for further detail on performing sensitivity analysis for HyTopS method.

Note that it would be interesting to compare the proposed method in this study with a density-based TO scheme that uses a full model. In previous studies, the basic GRO model has been verified and validated with both experiment and FLUENT [3, 40, 46, 47] and we observed good agreements between the thermal responses. Thus, we do not expect to see a significant improvement in thermal response if a full model is being used. In terms of hydraulic response, the previous study in [3] shows that ignoring the round corners in this model can result in up to 20% discrepancy in the computed pressure drop compared to the experiment. Not being able to consider the round corners in this model can be counted as one of the limitations in comparison with a full model. In terms of topology, orientation, and the number of microchannels, our proposed TO method is limited to the design of the pre-defined locations for microchannels. Nevertheless, achieving the same or higher resolution with a continuum-type FE model would require an extremely high resolution FE model to simulate the small microchannels considered [33].

5 Verification

The verification of the geometrical reduced-order finite element method (GRO-FEM), sensitivity analysis, and optimization algorithm are crucial factors in developing a topology optimization methodology. In this section, we first verify the GRO-FEM in-house code developed in this study in Section 5.1. We then verify the proposed topology optimization scheme in Section 5.2.

5.1 Verification of thermal solver

As mentioned earlier, the thermal model used in this study is a geometrical reduced-order (GRO) model. The primary reason for selecting a GRO thermal solver is that the main goal of this study is design, which is an iterative process, thus having a solver with a small computational cost and sufficient accuracy is our priority. The assumptions associated with the thermal model used in this study are presented in Section 2. First, we justify the assumptions underlying the thermal model, then we verify our finite element thermal model with the commercial finite element software, ANSYS/FLUENT.

For justification purposes, we consider the optimized solution obtained in Problem UHF1 in Section 4.1. The flow is assumed to be laminar. To justify this assumption, we need to compute the Reynolds number. Considering $\dot{V}_{in} = 22.5 \text{ ml/min}$, $D = 450 \text{ }\mu\text{m}$, and at the average temperature of the

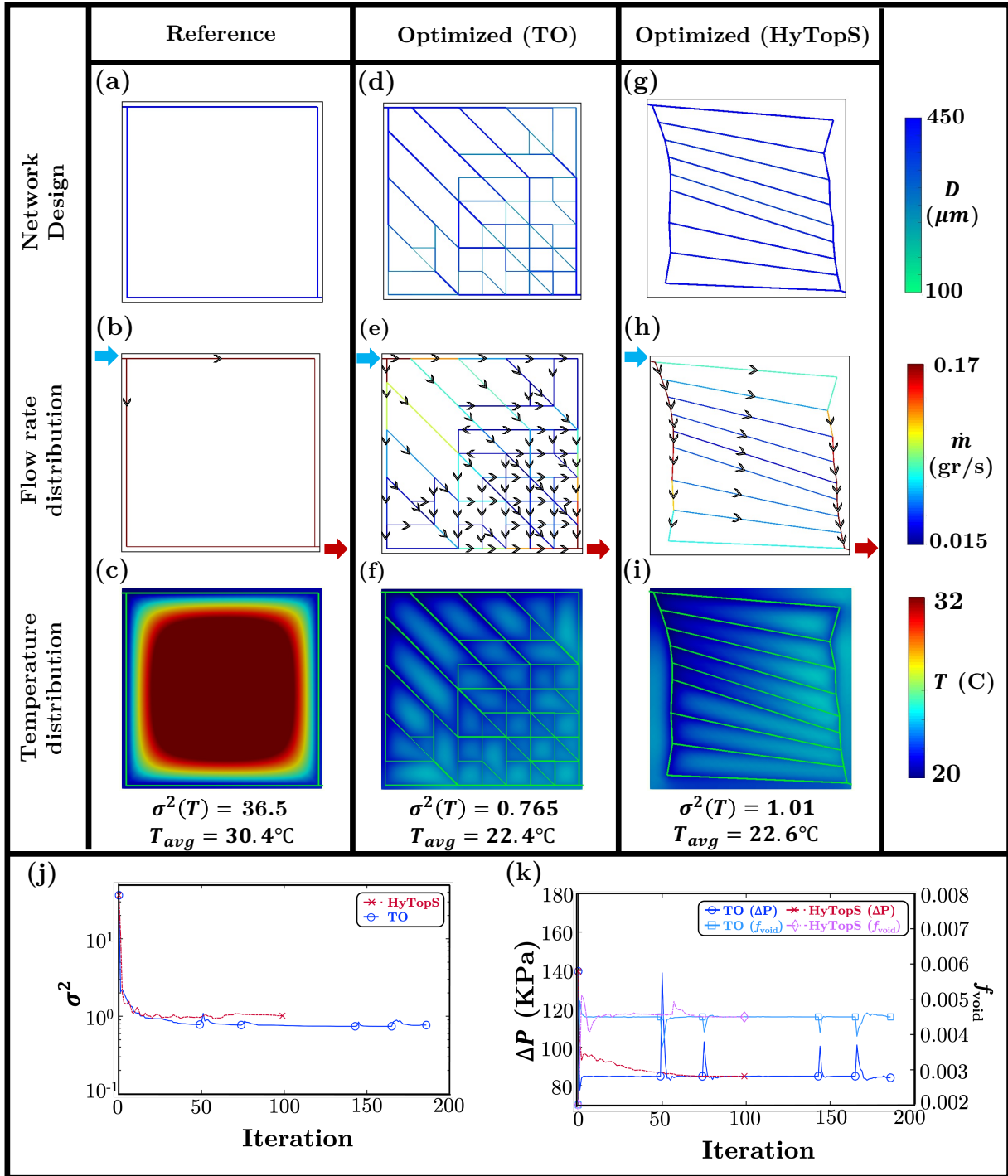


Fig. 11: (a) Reference design and its (b) mass flow rate and (c) temperature distributions. Optimized design, flow rate and temperature distributions obtained from (d, e, f) TO and (g, h, i) HyTopS schemes for the optimization problem of Section 4.2 using variance as the objective function. History plots of (m) the objective function and (n) the pressure drop and volume fraction constraints. Note: The optimization problem is subjected to a maximum pressure drop constraint of 85 KPa and maximum void volume fraction of 0.0045. Note that for the TO scheme, the objective value is 0.78 at the end of the continuation method with $\eta = 1$, and then remains at 0.77 for the optimized solution of the next steps of the continuation method.

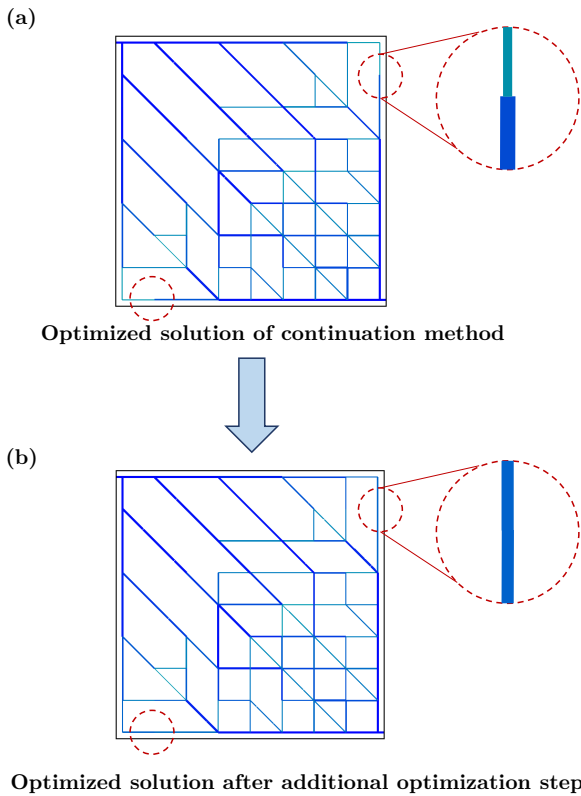


Fig. 12: The microchannel network obtained from the TO scheme in the optimization problem of Fig. 11: (a) at the end of continuation method and (b) after applying the additional optimization step explained in Fig. 2. The non-consistent diameter changes for microchannel connections are removed by using the additional optimization step.

fluid ($\approx 23^\circ\text{C}$), the Reynold number is almost 203, which verifies our assumption.

The other assumption in our GRO thermal model is that the microchannels are collapsed into line source/sinks due to their small diameter to length ratios. For this assumption to be valid, the mixed-mean fluid temperature T_m needs to be approximately equal to the microchannel wall temperature T_w . We can compute the difference between the wall temperature and mixed-mean temperature for fully developed, steady-state laminar flow as $\Delta T_{wm} \approx (\int f dA_p) / (\pi \kappa_c L_{ch} Nu)$, where A_p is the surface area of the panel, Nu is the Nusselt number, and L_{ch} is the length of the microchannel, respectively. Nusselt number is equal to 4.36 for fully developed fluid flow through a circular cross-section subjected to a constant heat flux [53]. For $L_{ch} = 1.037 \text{ m}$ and $A_p = 0.01 \text{ m}^2$, ΔT_{wm} is approximately $\approx 0.84^\circ\text{C}$. Note that in deriving this equation, we assume that the total heat absorbed in the domain is convected out through the microchannel network and we ignore the role of convection with the ambient environment, thus the actual difference between the wall and the

fluid mixed-mean temperature is lower than the predicted value.

We also assumed that the axial conduction of the coolant is negligible compares to the axial advection. The Péclet number is approximately equal to $\approx 8481 \gg 1$. Thus, we can conclude that the advective term dominates and the assumption of neglecting axial conduction of the coolant is valid. Note that in this model, the effect of corner radiuses is ignored. Based on the previous study in [3], this simplification may be one of the reasons for the observed discrepancy (up to 20%) between the pressure drop computed in the experiment and this model.

In terms of verification of thermal solver, Figure 13 (b, c) show the temperature distributions of the optimized design of UHF1 obtained from our finite element thermal solver and FLUENT, respectively. Note that for FLUENT, we considered the problem as three-dimensional with the same boundary conditions as defined for the problem UHF1. We define several measures such as (i) maximum temperature (T_{max}), (ii) average temperature (T_{avg}), and (iii) cooling efficiency ($\eta_c = \dot{m}c_p\Delta T / \int f dA_p$) to quantitatively compare the solution obtained from our GRO thermal solver and FLUENT. Table 3 summarizes the results of this comparison. The error presented in Table 3 is computed as the ratio of the difference between the amounts predicted by the GRO-FEM Code and FLUENT over the calculated value in FLUENT. The small amount of errors in all of these measures (0.4% – 3.4%) helps us to conclude that the temperature distribution obtained by the in-house GRO-FEM Code has acceptable accuracy. It is also worth mentioning that the run time for a single analysis with our GRO-FEM is less than a minute on a single thread. In contrast, the time spent for the mesh generation in ANSYS and the FLUENT simulation is several hours on a single thread. Thus, using the GRO-FEM significantly reduces the computational cost for each thermal analysis.

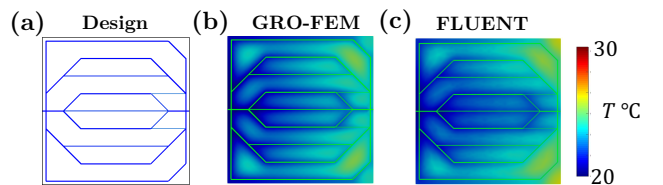


Fig. 13: (a) Optimized network design obtained in UHF1 optimization problem in Section 4.1. Temperature distributions obtained by (b) GRO-FEM and (c) FLUENT.

5.2 Verification of optimization algorithm

To confirm that each design solution has superior performance for the model parameters they were optimized for

Table 3: Comparison between the results obtained from GRO-FEM code and FLUENT.

Measures	GRO-FEM Code	FLUENT	Error
$T_{max} (^{\circ}C)$	25.3	26.2	3.4%
$T_{avg} (^{\circ}C)$	22.5	22.6	0.4%
η_c	88.3%	86.3%	2.3%

(i.e. confirming quality and consistency of the optimization results), we perform a cross-check. To do so, we design an optimization problem and repeat it three times for three different inlet volume flow rates (4, 10, and 20 ml/min). Except for the inlet volume flow rate, all of the material properties and simulation parameters are the same as the UHF1 problem presented in Section 4.1. The objective function is the p -mean temperature of the panel and the only constraint is on the maximum void volume fraction ($f_{void} \leq 0.0025$). In this problem, the loading and boundary conditions are symmetric with respect to the horizontal central line. Thus, we impose symmetric boundary condition on the central line and solve only the upper half of the panel.

The optimization results are presented in Fig. 14. As shown in Fig. 14 (d), (j), and (p) three different optimized designs are obtained by performing topology optimization process using $\dot{V}_{in} = 4, 10,$ and $20 ml/min$, respectively. The maximum temperature of the panel in the optimized solutions is reduced by 9.0% for $\dot{V}_{in} = 4 ml/min$, 21.9% for $\dot{V}_{in} = 10 ml/min$, and 28.5% for the inlet volume flow rate of 20 ml/min .

The temperature distributions of the designs in Fig. 14 (d), (j), and (p) are re-evaluated under inlet volume flow rates different from the design value and the cross-check results are shown in Fig. 15 and Table 4. As it was expected, each design performs best under the inlet volume flow rate for which it is optimized, thus we justified the effectiveness of the topology optimization.

To further verify the optimization algorithm, we need to show that the design solution is not trapped in the local minima. Indeed, due to the non-convex nature of the gradient-based topology optimization method, there exist multiple local minima. To address this issue, we created 30 distinct initial guesses for the optimization problem with an inlet volume flow rate of 20 ml/min . The results are shown in Fig. 16. All of the cases for this problem converges to the optimized, p -mean temperature of 20.92 ± 0.08 $^{\circ}C$. Thus, it can be concluded that the optimized solution of the case with the inlet volume flow rate of 20 ml/min converge to the optimize value.

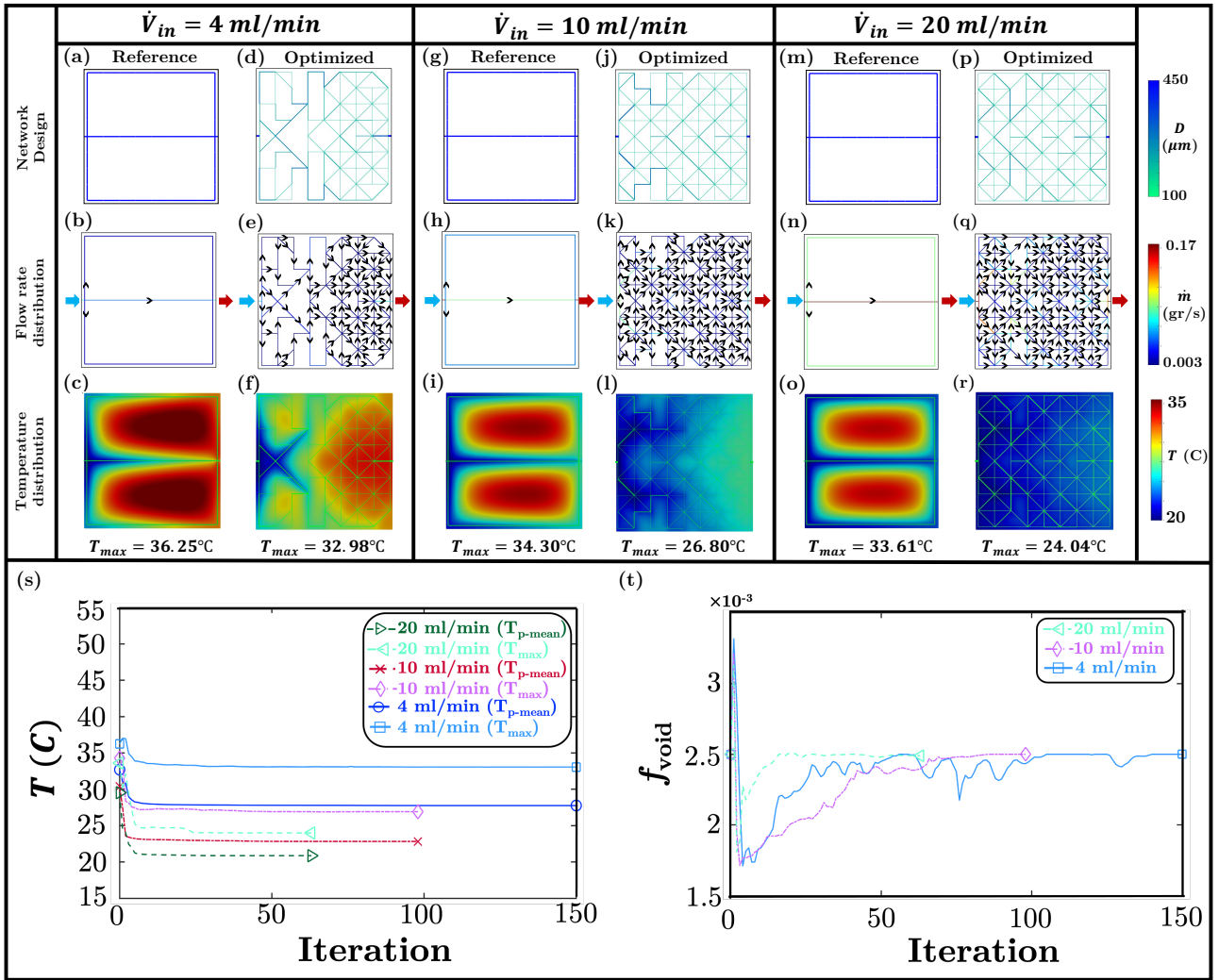


Fig. 14: Diameter, flow rate, and temperature distributions of the optimization problem in Section 5.2 for (a-f) $\dot{V}_{in} = 4 \text{ ml/min}$, (g-l) $\dot{V}_{in} = 10 \text{ ml/min}$, and (m-r) $\dot{V}_{in} = 20 \text{ ml/min}$. History plots of (s) objective function and (t) void volume fraction constraint. The problem is subjected to a constraint on the maximum void volume fraction of 0.0025.

Table 4: Cross-check of the optimization results of the optimization problem in Section 5.2. Each design performs best under the inlet volume flow rate for which it is optimized (Bold values).

Design by	Measures	Re-evaluated at $\dot{V}_{in} = 4 \text{ ml/min}$	Re-evaluated at $\dot{V}_{in} = 10 \text{ ml/min}$	Re-evaluated at $\dot{V}_{in} = 20 \text{ ml/min}$
$\dot{V}_{in} = 4 \text{ ml/min}$	Objective Function ($^{\circ}\text{C}$)	27.69	23.19	21.28
	T_{max} ($^{\circ}\text{C}$)	32.98	26.93	24.29
$\dot{V}_{in} = 10 \text{ ml/min}$	Objective Function ($^{\circ}\text{C}$)	27.81	22.79	20.98
	T_{max} ($^{\circ}\text{C}$)	33.30	26.80	24.07
$\dot{V}_{in} = 20 \text{ ml/min}$	Objective Function ($^{\circ}\text{C}$)	27.86	22.98	20.92
	T_{max} ($^{\circ}\text{C}$)	33.35	27.09	24.04

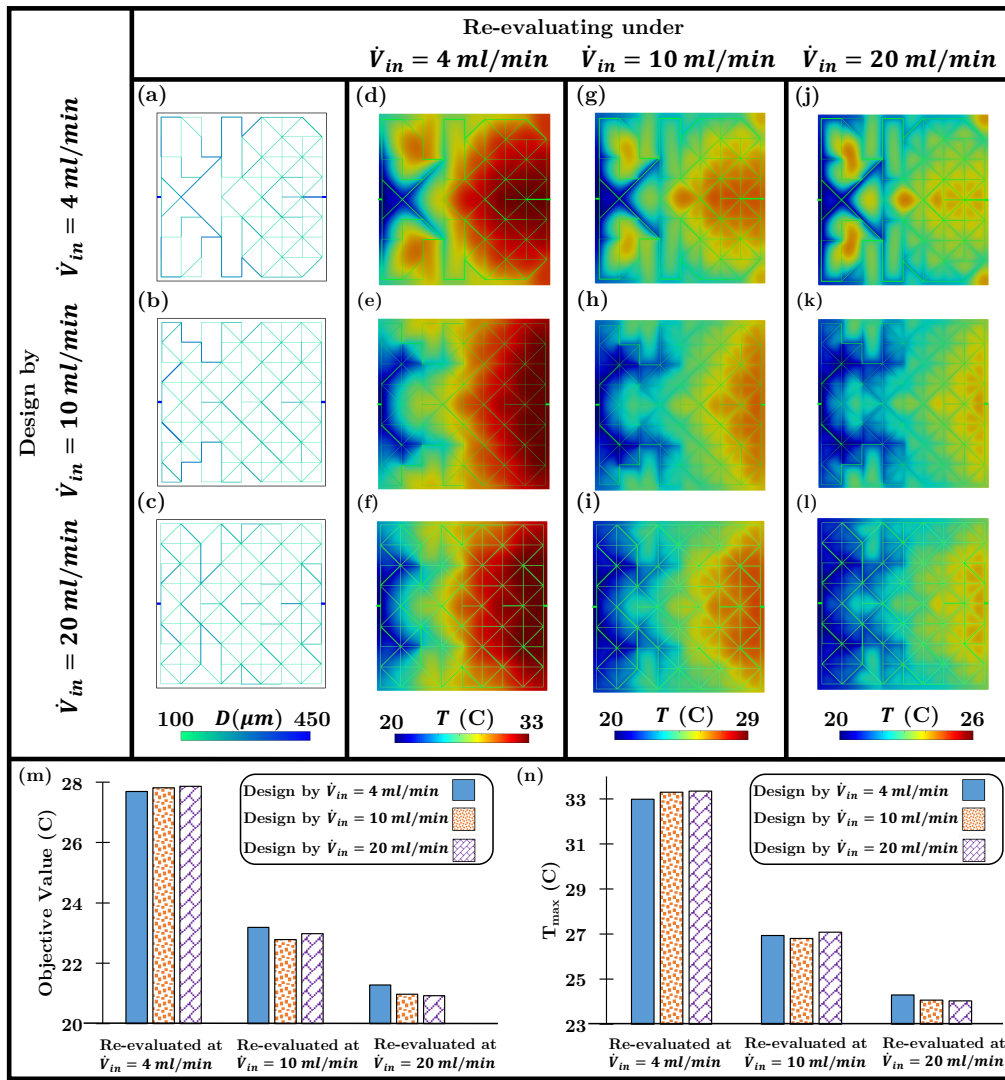


Fig. 15: (a, b, and c) Optimized designs under the inlet volume flow rates of 4, 10, and 20 ml/min. Temperature distributions of the design are re-evaluated under (d, e, and f) $\dot{V}_{in} = 4 \text{ ml/min}$, (g, h, and i) $\dot{V}_{in} = 10 \text{ ml/min}$, and (j, k, and l) $\dot{V}_{in} = 20 \text{ ml/min}$. Cross-check results for the (m) objective function and (n) maximum temperatures. Each design performs best under the inlet volume flow rate for which it is optimized.

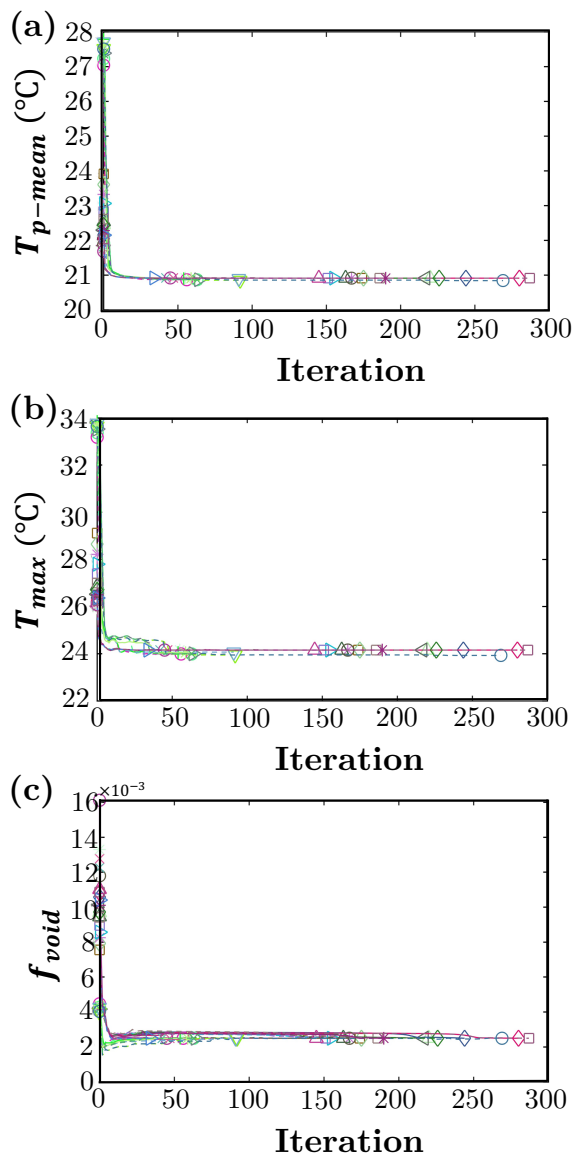


Fig. 16: Evolution of the (a) objective function, (b) maximum temperature, and (c) void volume fraction during the topology optimization starting from 30 random reference designs. All of them converge to the optimized, p -mean temperature of 20.92 ± 0.08 °C.

Conclusion

A gradient-based topology optimization methodology is presented to optimize actively-cooled microvascular composites. Using a geometrical reduced-order (GRO) thermal/hydraulic model enables us to collapse the microchannels into line source/sinks. This feature allows for finding the boundaries of the microchannels explicitly. By defining a new set of design parameters analogous to the design variables defined in the SIMP method, the optimizer finds the optimized design layout. The most important findings of the study have been listed in the following:

- With reference to the verification studies performed in Sections 5.1, we conclude that the GRO-FEM in-house code developed in this study is efficient and shows acceptable accuracy.
- The optimization methodology is suited for solving the optimization problems for actively-cooled microvascular composites, as the optimized solutions are verified by cross-check studies in Section 5.2.
- Our results reveal that the optimized design obtained by the presented TO scheme outperforms the designs of HyTopS and SO methods in terms of having a lower maximum and average temperatures, higher temperature uniformity, and having a more redundant network.
- The design solutions obtained by the topology optimization methodology outperform the benchmark design solutions by up to 59% in terms of having a lower maximum temperature.
- While this study concentrated on the active-cooling application, we expect the design framework will be applicable to a variety of physical phenomenon including structural and electromagnetic problems.

Replication of results

We provided comprehensive implementation detail, as a result, we are confident that the design methodology is reproducible. For this reason, we have decided not to publish the code. If the information provided in the paper is not sufficient, readers are welcome to contact the authors for further explanations.

Conflict of interest

The authors declare that they have no conflict of interest.

Acknowledgements

This work has been supported by Drexel University Career Development and Summer Research Awards. The authors ac-

knowledge the high-performance computing resources (PROTEUS: the Drexel Cluster) and support at the Drexel University. The authors also acknowledge the support from the Villum Foundation through the VILLUM Investigator Project InnoTop.

Appendix A

In this study, we aim to minimize the maximum temperature of the domain. However, the maximum temperature is not differentiable and as it is mentioned in Section 3, we replace it with a differentiable alternative, i.e. p -mean temperature. The p -mean temperature converges to the maximum temperature when p approaches infinity, i.e. $\lim_{p \rightarrow \infty} \|T\|_p = T_{max}$. However, using large values for p can be problematic. First of all, since we use the Gauss-Dunavant quadrature [54] to precisely calculate the integration of p -mean temperature, the larger values of p require more quadrature points which increases the computational cost. Moreover, the large values of p , make the p -mean temperature ill-conditioned or less smooth. Small values of p can also be problematic. Choosing a small value for p may not enable $\|T\|_p$ to capture reliably the trend in T_{max} . This issue may lead to local areas of high temperature similar to the stress concentration regions in the structural optimization problems.

In this section, we consider the reference design of CHF1 problem in Section 4.1. The maximum temperature of the panel in this design is 76.1°C. We evaluate the value of p -mean temperature using p equal to 2, 5, 8, 10, 12, 17, and 19. The number of quadrature points that we need to consider based on Gauss-Dunavant quadrature [54] are 3, 7, 16, 33, 61, and 73 for p equal to 2, 5, 8, 10, 12, 17, and 19, respectively. To compute the percent of the difference between the maximum temperature and p -mean temperature, we define a variable $T_d = (\|T_p\| - T_{max})/T_{max}$. Figure 17 compares the values of percent of the difference between the p -mean and maximum temperatures (T_d) and the number of quadrature points (N_Q) for different values of p . Based on the results, we decided to select $p = 10$ in this study. Note that we did not observe the problems of smoothness and being ill-conditioned for $\|T_p\|$ with $p = 10$ in the problems solved in this study.

Appendix B

As explained in the main text, the major role of D_{min} in (10) is preventing numerical issues. But we need to make sure that the value that we choose for D_{min} would not adversely impact the objective value. Thus, to find suitable value for D_{min} , we considered the reference design of each problem and we computed the amount of error produced in the value of the objective function when we consider a nonzero value for minimum diameter. We define the error

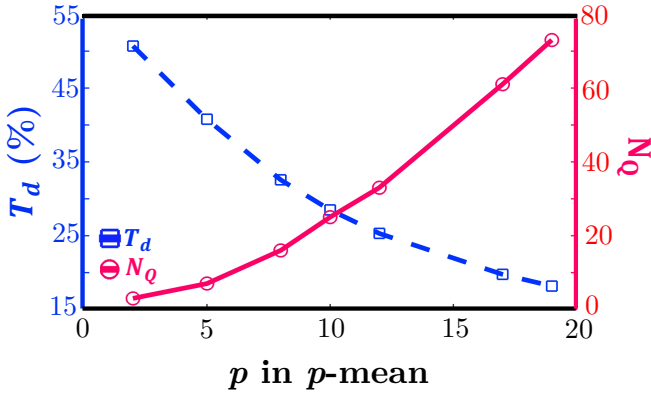


Fig. 17: The percent of difference between the maximum and p -mean temperatures of the domain (T_d) and the number of required Gauss-Dunavant quadrature points for different values of p in the p -mean.

as $e = (|\theta^{(@ D_{min}=0)} - \theta^{(@ D_{min} \neq 0)}|) / \theta^{(@ D_{min}=0)}$. Obviously, if the minimum diameter is zero, the amount of error will be zero and as the minimum diameter increases, the amount of error rises. Figure 18 shows the results for the reference designs of UHF1 and CHF1. Based on the presented results, we select $60 \mu\text{m}$ and $40 \mu\text{m}$ for the minimum diameter of the problems UHF1 and CHF1, respectively. The amount of error (e) until these two values are less than 0.01%.

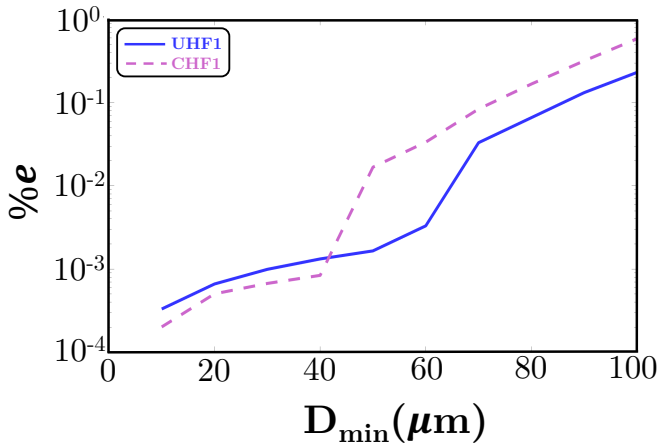


Fig. 18: The percent of error amount of error produced in the value of objective function when we consider a nonzero value for minimum diameter for the reference designs of UHF1 and CHF1 problems.

Appendix C

In this section, we aim to investigate the effect of removing the microchannels with the flow rates lower than a certain threshold on the objective function for the optimization problem UHF1 solved in Section 4.1. For that problem, we select a mass flow rate threshold of $3 \cdot 10^{-3} \text{ gr/s}$. We reevaluate the p -mean temperature value for all of the designs obtained in each iteration of the optimization problem UHF1 before removing the microchannels. Figure 19 compares the p -mean temperature values obtained from the cases where we remove the low mass flow rate microchannels with the cases where we do not remove any microchannel. The results are very close to each other. Thus, we can conclude that removing the microchannels with the mass flow rates lower than the prescribed threshold has a negligible effect on the p -mean temperature value.

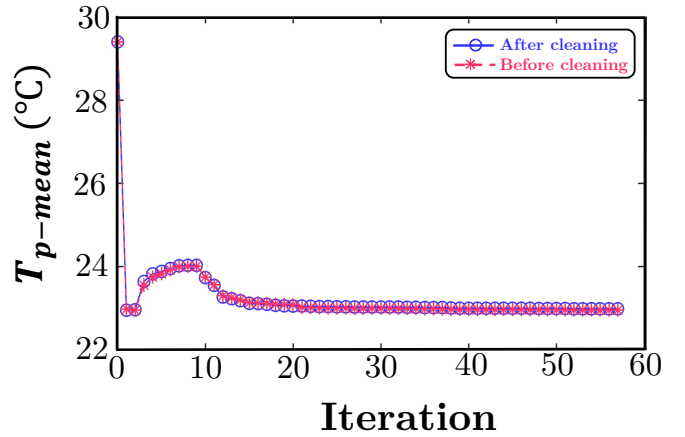


Fig. 19: Comparison of the p -mean temperature values obtained from the cases where we removed the low mass flow rate microchannels with the cases where we do not remove any microchannel.

Appendix D

A verification study of the analytic adjoint sensitivity analysis is performed by comparing the computed sensitivity with the central finite difference method for the reference design of the problem UHF1 in Section 4.1. The error between the adjoint and finite difference sensitivity analysis is given by $\varepsilon = \left| \frac{((d\theta/d\alpha)^{Adj} - (d\theta/d\alpha)^{FD})}{(d\theta/d\alpha)^{Adj}} \right|$, where $|*|$ indicates the absolute value of $*$, and superscripts of Adj and FD indicate adjoint method and finite difference approach, respectively. The error is plotted in Fig. 20 for a sequence of perturbations

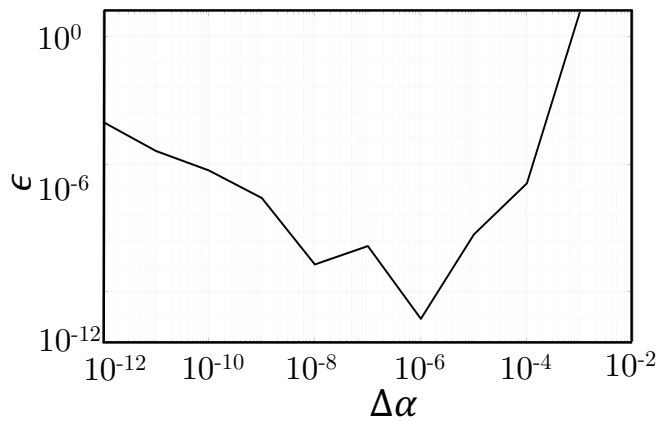


Fig. 20: The relative error, ϵ , between the adjoint sensitivity analysis in Section 3 and approximated central finite difference sensitivity plotted as function of the magnitude of the perturbation in the design parameter, $\Delta\alpha$. The relative error has small value, which indicates that the sensitivity analysis is correctly derived and implemented.

from $\Delta\alpha = 10^{-2}$ to 10^{-12} . The amount error is very small ($\approx 10^{-11}$) and we can conclude that the sensitivity analysis is correctly derived and implemented in this study.

References

1. A.P. Esser-Kahn, P.R. Thakre, H. Dong, J.F. Patrick, V.K. Vlasko-Vlasov, N.R. Sottos, J.S. Moore, S.R. White, *Advanced Materials* **23**(32), 3654 (2011)
2. S.J. Pety, M.H.Y. Tan, A.R. Najafi, P.R. Barnett, P.H. Geubelle, S.R. White, *International Journal of Heat and Mass Transfer* **115**, 513 (2017)
3. M.H.Y. Tan, A.R. Najafi, S.J. Pety, S.R. White, P.H. Geubelle, *International Journal of Heat and Mass Transfer* **103**, 594 (2016)
4. A. Coppola, A. Griffin, N. Sottos, S. White, *Composites Part A: Applied Science and Manufacturing* **78**, 412 (2015)
5. A. Bejan, *International Journal of Heat and Mass Transfer* **40**(4), 799 (1997)
6. Y. Hadad, B. Ramakrishnan, R. Pejman, S. Rangarajan, P.R. Chiarot, A. Pattamatta, B. Sammakia, *Applied Thermal Engineering* **150**, 720 (2019)
7. S. Soghrati, A.R. Najafi, J.H. Lin, K.M. Hughes, S.R. White, N.R. Sottos, P.H. Geubelle, *International Journal of Heat and Mass Transfer* **65**, 153 (2013)
8. X. Dong, X. Liu, *Numerical Heat Transfer, Part A: Applications* **77**(1), 90 (2020)
9. Y. Hadad, R. Pejman, B. Ramakrishnan, P.R. Chiarot, B.G. Sammakia, in *2018 17th IEEE Intersociety Conference on Thermal and Thermomechanical Phenomena in Electronic Systems (ITherm)* (IEEE, 2018), pp. 673–682
10. J.S. Lee, S.Y. Yoon, B. Kim, H. Lee, M.Y. Ha, J.K. Min, *International Journal of Heat and Mass Transfer* **172**, 121172 (2021)
11. P. Li, Y. Liu, T. Zou, J. Huang, *Advances in Mechanical Engineering* **9**(7), 1687814017708175 (2017)
12. A.M. Aragón, R. Saksena, B.D. Kozola, P.H. Geubelle, K.T. Christensen, S.R. White, *Journal of Computational Physics* **233**, 132 (2013)
13. S. Ozguc, L. Pan, J.A. Weibel, *International Journal of Heat and Mass Transfer* **169**, 120896 (2021)
14. Y. Hadad, S. Rangarajan, K. Nemati, B. Ramakrishnan, R. Pejman, P.R. Chiarot, B. Sammakia, *International Journal of Thermal Sciences* **148**, 106145 (2020)
15. T. Matsumori, T. Kondoh, A. Kawamoto, T. Nomura, *Structural and Multidisciplinary Optimization* **47**(4), 571 (2013)
16. H. Rodrigues, P. Fernandes, *International Journal for Numerical Methods in Engineering* **38**(12), 1951 (1995)
17. S. Yan, F. Wang, O. Sigmund, *International Journal of Heat and Mass Transfer* **122**, 660 (2018)
18. L.H. Olesen, F. Okkels, H. Bruus, *International Journal for Numerical Methods in Engineering* **65**(7), 975 (2006)
19. N. Wiker, A. Klarbring, T. Borrvall, *International journal for numerical methods in engineering* **69**(7), 1374 (2007)
20. G.H. Yoon, *Journal of Mechanical Science and Technology* **24**(6), 1225 (2010)
21. A.A. Koga, E.C.C. Lopes, H.F.V. Nova, C.R. De Lima, E.C.N. Silva, *International Journal of Heat and Mass Transfer* **64**, 759 (2013)
22. G. Marck, M. Nemer, J.L. Harion, *Numerical Heat Transfer, Part B: Fundamentals* **63**(6), 508 (2013)
23. K. Yaji, M. Ogino, C. Chen, K. Fujita, *Structural and Multidisciplinary Optimization* **58**(2), 817 (2018)
24. S.B. Dilgen, C.B. Dilgen, D.R. Fuhrman, O. Sigmund, B.S. Lazarov, *Structural and Multidisciplinary Optimization* **57**(5), 1905 (2018)
25. J. Alexandersen, N. Aage, C.S. Andreasen, O. Sigmund, *International Journal for Numerical Methods in Fluids* **76**(10), 699 (2014)
26. J. Asmussen, J. Alexandersen, O. Sigmund, C.S. Andreasen, *Structural and Multidisciplinary Optimization* **59**(4), 1105 (2019)
27. M. Zhou, H. Lian, O. Sigmund, N. Aage, *International Journal for Numerical Methods in Fluids* **88**(6), 296 (2018)
28. S. Yan, F. Wang, J. Hong, O. Sigmund, *International Journal of Heat and Mass Transfer* **143**, 118462 (2019)
29. X. Dong, X. Liu, *Chemical Engineering Journal* **412**, 128594 (2021)
30. A. Jarrett, I.Y. Kim, *Journal of Power Sources* **196**(23), 10359 (2011)
31. T. Borrvall, J. Petersson, *International journal for numerical methods in fluids* **41**(1), 77 (2003)
32. A. Gersborg-Hansen, M.P. Bendsøe, O. Sigmund, *Structural and multidisciplinary optimization* **31**(4), 251 (2006)
33. X. Zhao, M. Zhou, O. Sigmund, C.S. Andreasen, *International Journal of Heat and Mass Transfer* **116**, 1108 (2018)
34. J.K. Guest, J.H. Prévost, *International Journal for Numerical Methods in Engineering* **66**(3), 461 (2006)
35. A.R. Najafi, M. Safdari, D.A. Tortorelli, P.H. Geubelle, *International Journal for Numerical Methods in Engineering* **111**(10), 927 (2017)
36. A.R. Najafi, M. Safdari, D.A. Tortorelli, P.H. Geubelle, *Computer Methods in Applied Mechanics and Engineering* **296**, 1 (2015)
37. A.R. Najafi, M. Safdari, D.A. Tortorelli, P.H. Geubelle, *International Journal for Numerical Methods in Engineering* (2020)
38. M.H.Y. Tan, M. Safdari, A.R. Najafi, P.H. Geubelle, *Computer Methods in Applied Mechanics and Engineering* **283**(1), 1382 (2015)
39. M. Safdari, A.R. Najafi, N.R. Sottos, P.H. Geubelle, *Journal of Computational Physics* **318**, 373 (2016)
40. R. Pejman, S.H. Aboubakr, W.H. Martin, U. Devi, M.H.Y. Tan, J.F. Patrick, A.R. Najafi, *International Journal of Heat and Mass Transfer* **144**, 118606 (2019)
41. R. Pejman, V. Keshavarzadeh, A.R. Najafi, *Computer Methods in Applied Mechanics and Engineering* **375**, 113624 (2021)
42. R. Pejman, E. Maghami, A.R. Najafi, *Applied Thermal Engineering* **181**, 115916 (2020)
43. M. Bahrami, M. Yovanovich, J. Culham, in *ASME 3rd International Conference on Microchannels and Minichannels* (American Society of Mechanical Engineers, 2005), pp. 269–280

44. R. Shah, A. London. Laminar flow forced convection in ducts (a sourcebook for compact heat transfer exchange analytical data) (1978)
45. A.N. Brooks, T.J. Hughes, Computer methods in applied mechanics and engineering **32**(1-3), 199 (1982)
46. S.J. Pety, M.H.Y. Tan, A.R. Najafi, A.C. Gendusa, P.R. Barnett, P.H. Geubelle, S.R. White, Applied Thermal Engineering **131**, 965 (2018)
47. M.H.Y. Tan, A.R. Najafi, S.J. Pety, S.R. White, P.H. Geubelle, Applied Thermal Engineering **135**, 145 (2018)
48. J. Petersson, O. Sigmund, International Journal for Numerical Methods in Engineering **41**(8), 1417 (1998)
49. A. Asadpoure, M. Tootkaboni, J.K. Guest, Computers & Structures **89**(11-12), 1131 (2011)
50. W. Aichtziger, M. Stolpe, Computational Optimization and Applications **44**(2), 315 (2009)
51. MATLAB, *version 8.5 (R2015a)* (The MathWorks Inc., Natick, Massachusetts, 2015)
52. R. Pejman, A.R. Najafi, in *ASME 2020 International Design Engineering Technical Conferences and Computers and Information in Engineering Conference* (American Society of Mechanical Engineers Digital Collection, 2020)
53. W.M. Kays, M.E. Crawford, B. Weigand, *Convective heat and mass transfer* (McGraw-Hill, 2005)
54. D. Dunavant, International journal for numerical methods in engineering **21**(6), 1129 (1985)